Department of Precision and Microsystems Engineering

Design and optimization of a Tubular Linear Motor intended for low-duty CNC machines

T. Y. Kramer

Report no : 2020.059
Coach : Prof. J. Spronck
Professor : Prof. J. Spronck
Specialisation : HTE - Mechatronic System Design
Type of report : Final Thesis Report
Date : 14-12-2020

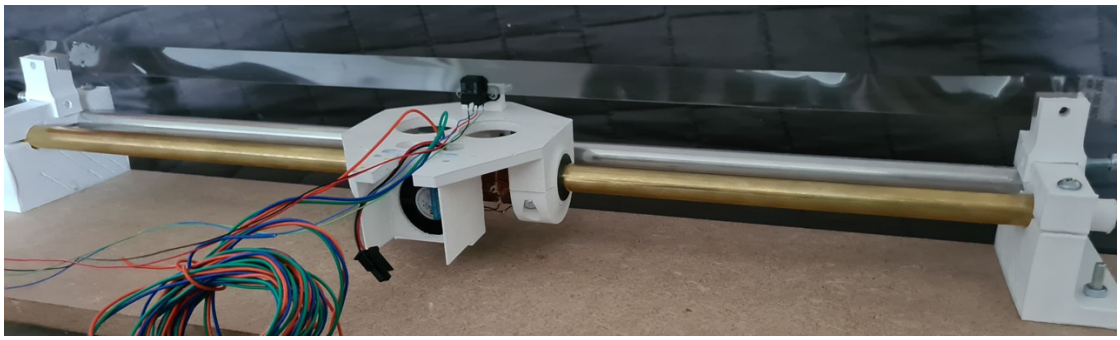

Preface & Motivation

Since I was young, I've always had ambitions to start my own company. I came up with many ideas, however none seemed prosperous until I studied the book: "The Design of High Performance Mechatronics", written by R. M. Schmidt. A single section explained how a Lorentz actuator could be extended, such that linear motion could be achieved. Given the pros of using this type of motor I was wondering why this hadn't been implemented yet in 3D printers or other CNC machines where low thrust is required.

Personally, I am a 3D print enthusiast and a 'maker'. I enjoy 3D modelling and consider myself creative in many ways. I decided to assign myself the mission to improve the effectiveness of additive manufacturing, in particular Fused Deposition Modelling 3D printers. This drive, allowed me to focus and achieve what I initially thought would be hard, but very fun to do. I'm very proud of what I have achieved, and can't wait what the future might bring regarding engineering and business.

Aside to working on this thesis during the year, I've participated in several business courses and competitions with this mission in mind. My partner and I were able to win price money, which was invested in the development of this project.

In the midst of the academic year, we've been plagued by the COVID-19 virus. This required adaptation, which affected my work in different manners. The pandemic introduced a 2-3 months study delay, due to changes within the university and due to component delivery delays, which were ordered from outside the country. Furthermore, I had it rough emotionally. Isolation and full-time working on this thesis introduced loneliness, however I pulled through with the help of family and friends.

I would like to thank Jo Spronck for being my supervisor. He had been incredibly helpful in not only coming up with systematic approaches, but also wanted to help me with business aspects. He has given me the support and freedom required for this project and had been a very entertaining supervisor. Thank you so much Jo, I will keep you updated with the development of my product!

I would also like to thank everyone of the Monday meeting sessions. The information I shared and input I received helped me improve my work. In particular, aside to Jo Spronck, I would like to thank Hassan Hossein, Andres Hunt and Niranjan Saikumar for providing me with interesting knowledge and criticism during these sessions. Every session I have participated in taught me something new, and it had been very interesting seeing other people's work. I'm interested to see where their careers are headed.

Finally I would like to thank my friends and family with their emotional and financial support throughout my entire study. Without their hard work and love I wouldn't be the person I am today, a very proud graduate engineer that is ready to take on the world!

T. Y. Kramer
Delft, December 2020

Abstract

Nowadays, Fused Deposition Modeling (FDM) 3D printers or CO2 laser cutting machines use a belt-driven design for positioning. In this design, a stepper motor drives a carriage using a belt as an elastic transmission. The design is a cost-effective set-up and can be used in open-loop, meaning no feed-back control scheme is required. However, this set-up brings several complications an engineer has to account or find solutions for.

The drive belt is elastic, resulting in belt stretch and induced vibrations, which ultimately reduces the total accuracy of the final manufactured product. This effect becomes more clear when the dimensions of the machine are up-scaled, resulting in longer belts whose stiffness scales in the best case inversely proportionally to the axis length. Since the stiffness is reduced, the acceleration of the drive system should also be reduced, such that the manufactured part is within requirements. However, acceleration is of great importance for fast manufacturing. Not only the accuracy suffers, but also the manufacturing speed. For FDM (Fused Deposition Modelling) 3D printing, an accuracy of 0.5 [mm] is found to be acceptable and to be of industrial grade, an accuracy of 0.2 [mm] is required [50]. The accelerations are limited accordingly. The required performance in this report is 1 $[m/s]$ at an acceleration of 10 $[m/s^2]$ with an accuracy that is close to industrial performance, which is for the reasons stated above impossible to achieve with the current belt-driven design.

Then there's the complexity of the drive system. The drive system utilizes several pulleys that have to be precisely positioned, such that the belt is straight and tightened within the requirements, which increases the total time required for assembly. Furthermore, mechanical wise, these parts introduce backlash; creep and wear. This further reduces the total repeatability of the drive system (over time) and thus requires regular maintenance.

For these reasons, a different method of actuation is considered to increase on print speed; accuracy and to reduce on assembly complexity. After researching different methods of actuation, it was found that direct-drive motors could innovate these machines. This means there's no longer an elastic or mechanical transmission, essentially resulting in a mass system that can be moved very fast and accurately. Furthermore, the amount of moving parts is reduced. The following thesis project is proposed: "The design and manufacturing of a low-cost direct-drive motor, that is specifically optimized for low-duty CNC machines in performance and cost". Research regarding these motor is performed based on commutation, control and motor types.

Linear stepper motors (reluctance motors) and linear motors (based on the Lorentz actuators) are found to be the most viable solutions as direct-drive actuators.

Where stepper motors are essentially DC in nature, and have many poles, it can be used in open-loop, reducing the complexity and thus cost of the system. These motors have a torque/-force advantage at low speeds, however quickly degrades at higher speeds. This is due to the power supply clipping because of the considerable induced back electromotive force at these speeds [10]. The torque/force further reduces exponentially when micro-stepping is introduced to increase on resolution [9]. Furthermore, since the motor and stator combined are of high mass due to iron, this set-up is not preferred.

On the other hand, linear motors seem to be a prosperous candidate. With no to little iron included, the self-induction is considerably less, which results in a fairly constant force/speed curve that is ideal for motor control [10]. The mass is considerably less, which requires less power and results in improved dynamics. The input nature of these motors is usually 3 phase current. The motor requires an encoder and a feed-back control loop, which increases the total cost of these motors. Depending on the motor type, these motors cost minimally € 700 per meter stroke (company Tecnotion) and when outsourced are either up- or downscaled while keeping the price high. To reduce the cost, low-cost components are used; smart design choices are implemented; low-cost manufacturing methods are used and the design is optimized in cost and performance.

It's been found that the iron-less tubular linear motor is the most prosperous candidate, because of its high efficiency; high actuator stiffness; no cogging; great heat dissipation; non-critical air gap; ease of manufacturing and a very wide speed range. Furthermore, the rotor can easily be incorporated in a carriage with sliding bearings, where the stator also acts as the guiding rod that is part of the gantry. This reduces the complexity of the gantry significantly.

Research regarding the commutation is performed, where State Vector Pulse Width Modulation (SVPWM) in combination with Field Oriented Control is implemented in a MATLAB SIMULINK model to drive the motor closed-loop. The controller is designed for 130 [Hz] bandwidth and operates at 500 [Hz]. The PWM signals operate at 20 [kHz], which is inaudible.

An analytical model of the iron-less tubular linear motor is presented, however a COMSOL finite-elements generator model provides more information regarding motor behavior. Furthermore a COMSOL motor model is developed to reduce on computation time that is used for extracting the motor constant and coil resistances.

Given the motor type; motor dimensions; wire size; physical properties; total maximum mass; maximum power; maximum current and required acceleration as constraints, an iron-less tubular linear motor has been designed in COMSOL and evaluated for 1536 different models, after which brute force optimization is performed in MATLAB to find the ideal coil and magnet dimensions. The objective of the optimization was to minimize the total mass (and thus cost) of the motor with a weight factor of 2, whereas heat is minimized with a weight factor of 1.

The maximum speed is set to be 1 [m/s] at an acceleration of 10 [m/s2], which results in up to 5 times faster print times (with better accuracy) compared to existing FDM 3D printers. Black box identification has been performed in order to tune the PD controller. The Damper of the controller is modified to use the derivative on measurement in order to counter derivative kick. The motor constant is estimated and verified to be about 3.75 N/A. The motor has an accuracy of 0.2 [mm] 3 σ for the given acceleration and speed and may be considered industrial. A low-cost optical quadrature encoder is used, that uses an encoder strip with very fine lines at

71.1 [μm] apart. This allows for a resolution of minimally [μm] micrometers. The total material cost including electronics is expected to be below 50 euros.

This final Thesis report helps pave a way for engineers to learn and manufacture linear motors, and specifically tubular linear motors. From A-Z, from initial research to final product. The report includes appendices and company appendices. The company appendices are named 'Appendix C#'.

Contents

Chapter 1

General Introduction

1.1 Context & Problem Statement

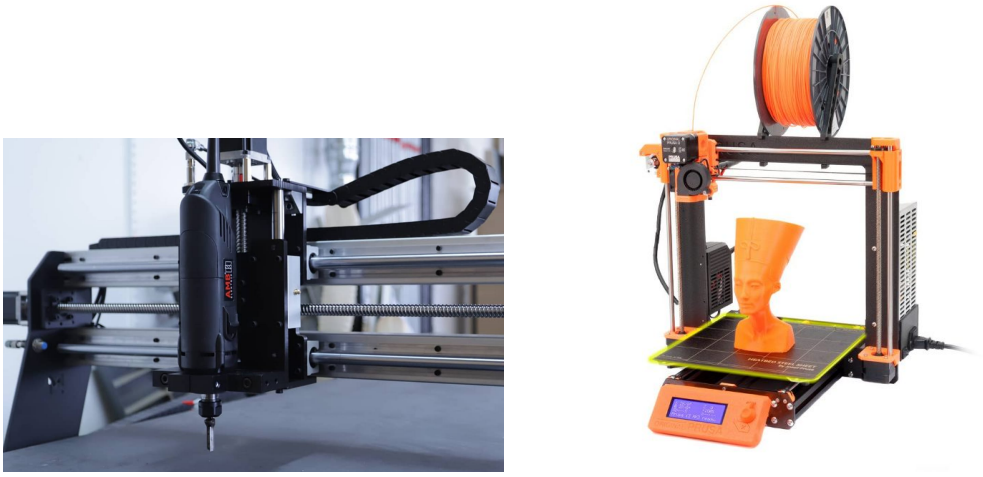

(a) **(b)**

Figure 1.1:
(a) CNC Milling machine, screw-driven: high-duty CNC machinery [30].
(b) CNC 3D printer, belt-driven: low-duty CNC machinery [46].

Automation is of great importance for this era, the 4th industrial revolution. In this field, the last few years we've seen a rise in so called 'desktop' machines for 3D printing; laser engraving/cutting and CNC (Computer Numerical Control) milling. Where CNC milling requires large cutting forces and thus may be considered a high-duty CNC machine (see figure 1.1a), 3D printing and laser cutting machines do not require powerful actuators and are considered to be low-duty CNC machines (see figure 1.1b).

Therefore, these low-duty CNC machines use a different drive system compared to the high-

duty CNC machines. Where high-duty CNC machines use a screw driven system, the low-duty CNC machines use a belt-driven system. In this design, a rotary stepper motor drives a belt, where the belt is connected to a carriage. The carriage is then allowed to move only in a single degree of freedom.

This set-up is cost-effective, since the components are widely available and the stepper motors are controlled in an open-loop fashion, not requiring a complex (expensive) feed-back control scheme. However, this set-up brings several complications an engineer has to account for or find solutions for.

Figure 1.2: Due to the limited stiffness of the belt of a belt-driven system, vibrations and belt stretch cause ringing in the final manufactured product. A similar effect is seen in laser cutting machines [31].

The belt is an elastic element. This allows for belt stretch, and since the plant is essentially a spring mass system (no damping due to visco-elasticity of the belt considered), vibrations and ringing further reduce the total accuracy of the manufactured part. This last effect is shown in fig. 1.2. This effect becomes more visible when the dimensions of the machine are up-scaled, resulting in longer belts. The belt's stiffness scale in the best case inversely proportionally to the axis length as show in formula 1.1. Here it's assumed the belt and the axis are of the same length. Where E [Pa] is the elastic young's modulus of the belt's material, A [m2] is the cross section and L [m] is the belt's length.

$$k = \frac{EA}{L} \tag{1.1}$$

However, as we see with different 3D printers, different set-ups result in different belt lengths 1.3. For example as for an Ultimaker FDM 3D printers, increasing the axis length, results in a belt that is twice the axis length. That is because the belt goes forth and back. Another drive system, the CoreXY (H-Bot) set-up, uses 2 stepper motors that are coupled to provide X and Y motion. This set-up reduces torque on the driven carriage, however scaling the axis length results in a drastic increase in belt length. The stiffness suffers, and the accelerations (and thus drive forces) are reduced accordingly to reduce ringing and belt stretch. An accuracy of 0.5 [mm] for desktop FDM 3D printers is considered to be acceptable, and for industrial 3D printers an accuracy of 0.2 [mm] is required [50].

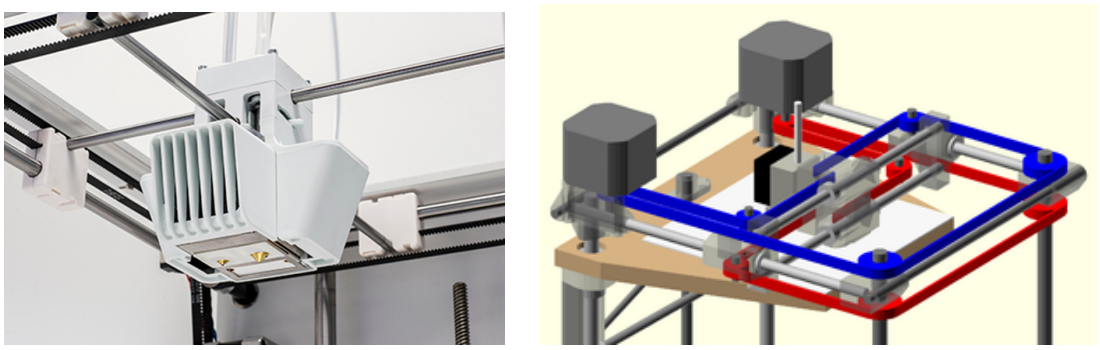

(a) (b)

Figure 1.3:
(a) An Ultimaker [62] drive system uses four belts, i.e. 2 for each axis.
(b) The RepRap CoreXY [49] drive system uses coupled motors. The belts are of significant length, especially when the machine is up-scaled.

The acceleration is the most significant factor for fast production, especially when small features are included in the production model. Thus the reduction in stiffness, not only reduces quality but also the production rate.

Then there's the complexity of the drive system. The drive system utilizes multiple pulleys that have to be precisely positioned, such that the belt is straight and tightened within the requirements, which increases the total time required for assembly. The belt has to be very tight, such that the eigen frequency and thus stiffness is of high value to reduce the effect of ringing. Furthermore, mechanical wise, these parts introduce backlash; creep and wear. This further reduces the total repeatability of the drive system (over time) and thus requires regular maintenance.

A solution would be to remove the elastic transmission all together and use a different set-up instead, which is discussed in the next section.

1.2 Existing Solutions

1.2.1 Screw-driven

One solution would be to increase the transmission's stiffness significantly by using a screw-driven system (see figure 1.4a). In this design a stepper or servo motor is used to drive a nut, that is connected to the rotating screw. The stiffness is several orders of magnitude larger, reducing ringing and elongation/compression significantly. The drive system can output large forces, and for that reason is being used in CNC milling. The set-up is cost-effective, since many parts are widely available. When stepper motors are used, the control complexity and the cost is further reduced.

However since the transmission is mechanical in nature. Wear and backlash are introduced in the system, which becomes more drastic at higher speeds. Regular maintenance is required, such as greasing and part replacement.

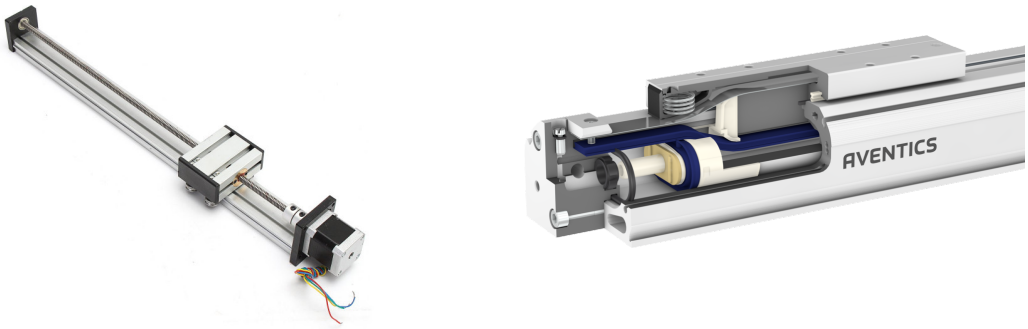

(a) (b)

Figure 1.4:
(a) A screw-driven system. Increases the drive stiffness [3].
(b) A pneumatic direct-drive system [2]; no mechanical transmission.

Since the drive system uses an additional screw, the total number of mechanical constraints has increased by at least 2, which may result in axis binding if not aligned properly. A better option would be to have no transmission between the motor and the axis, such that backlash; creep and wear is considerably less or non-present. These methods are called direct-drive solutions.

1.2.2 Pneumatics/Hydraulics

These machines use a fluid, whether that is a gas or liquid to provide thrust (see figure 1.4b). Large stroke and high thrust is achievable. Figure 1.4b shows an example of a pneumatic drive. By changing the pressure in the tube, the carriage is accelerated. Leakage is to be prevented, and the rubber seals may have to be replaced over time. The system requires closed-loop control in order to position accurately. Furthermore, a compressor is required to increase the tube's internal pressure. This significantly increases the cost and complexity of the system.

1.2.3 Linear Stepper, Reluctance Motors

Similarly to how a rotary stepper motor works, the motor consists of a rotor and a stator. However, unlike other linear motor designs, the stator is a passive component [14]. The stator, also called platen, is a (stainless) steel plate with slots milled into it. The rotor, also called the forcer, contains laminations with slotted teeth that are of high magnetic permeability; motor windings and a permanent magnet. The forcer teeth are typically offset by 1/4th tooth pitch to those of the platen, to ensure constant attraction is maintained and the next set of teeth comes in alignment when the current is switched. These teeth act as poles and the amount of poles range from 50-100 poles depending on the stepper, which allows for small step positioning in open-loop.

The attractive forces between the forcer and platen are considerable and a proper choice for the bearing is required to ensure the airgap remains constant.

The motor is easy to implement and can be run in open-loop. micro-stepping is used to reduce motor vibrations, which are induced by the DC input pulses that coincide with the natural

frequency of the motor. Resonance results in a loss of torque and may offset the teeth, resulting in reduced dynamics and repeatability. micro-stepping, such as half- or quarterstepping adds input levels (see figure 1.5a, such that the input pulses turn more into a sinusoid with every increase in micro-stepping level. However, this comes at a cost of torque/force, which decreases exponentially as can be seen in table 1.1 [9].

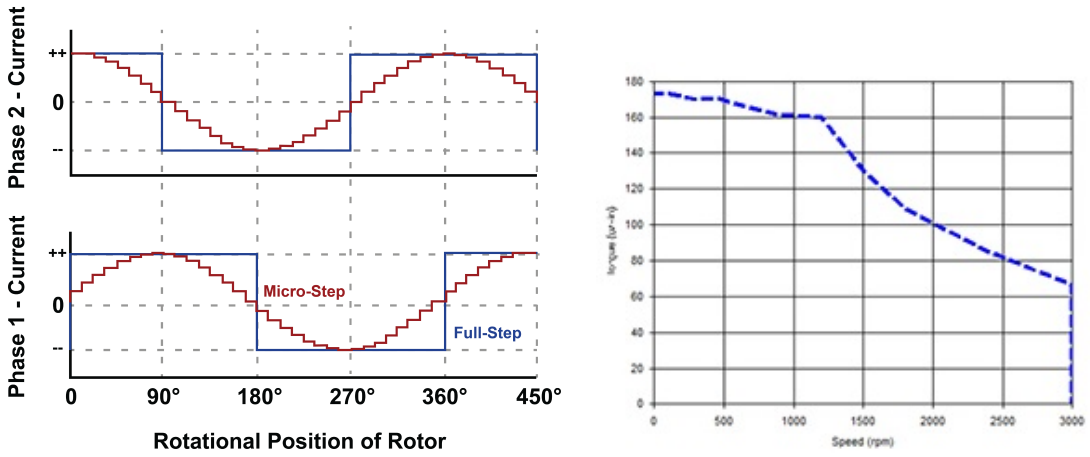

(a) (b)

Figure 1.5:
(a) Current waveform in a 2-phase stepper motor: micro-stepping vs full-step [9].
(b) Power supply clipping due to induced back electromotive force in the stepper phases (x: RPM/speed; y: torque/force output) [10].

Micro-step	% Holding force
None	100
2	70.71
4	38.27
8	19.51
16	9.8
32	4.91
64	2.45
128	1.23
256	0.61

Table 1.1: The effect of micro-stepping on the torque/force output of a stepper motor [9].

Furthermore, since the forcer has many 'poles' and iron, self-induction is significant at high speeds. This results in a back EMF (Electromotive Force), that counters the input bus voltage. At a certain speed, the power supply starts clipping, since it can no longer correct for this back EMF [10]. The result is a degrading force/speed curve as can be seen in fig 1.5b.

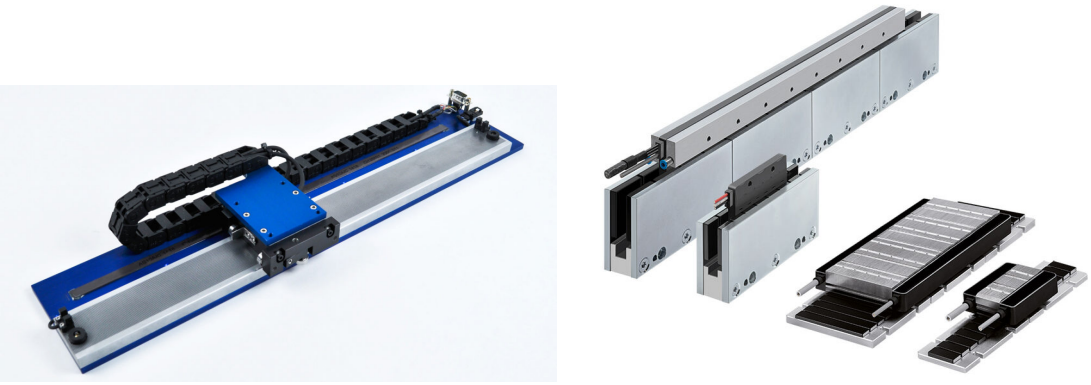

(a) (b)

Figure 1.6:
(a) Linear stepper motor consisting of a rotor and a platen that acts as stator [12].
(b) U-channel linear motors and an iron-core flat motor [19].

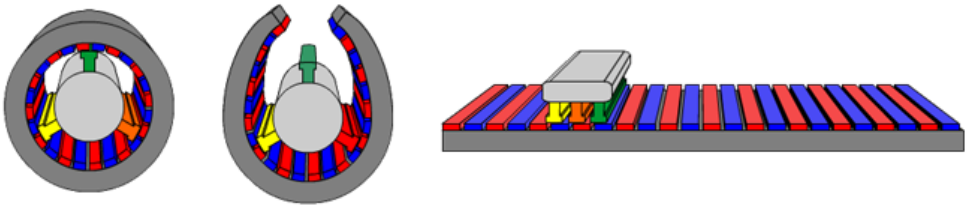

Figure 1.7: Unrolling a servo motor results in a linear flat motor [65].

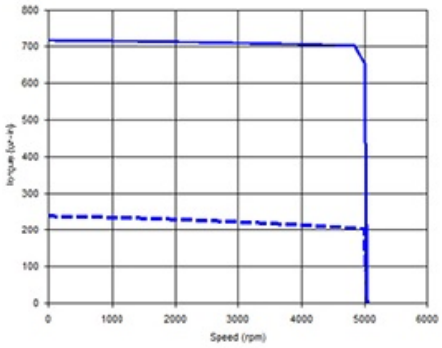

Figure 1.8: Unlike stepper motors, servo and linear motors have a fairly constant force/speed curve [10].

1.2.4 Linear Motors

Where linear stepper motors are the linear variant of rotary stepper motors, linear motors are the linear variant of servo motors. One may unroll a rotary servo motor, which results in a linear flat motor (see figure 1.7) [65]. Another way of viewing this type of motor, is by imagining

multiple Lorentz actuators after one another with magnets of changing polarity. The motors use the Lorentz force, whereas stepper motors make use of the reluctance/attractive force. A linear motor is unlike a stepper motor, AC in nature and has significantly less poles. Most often three phase current is fed to the coils of the rotor. The stator consists of permanent magnets with or without spacers, which introduces a magnetic wave. The rotor essentially rides the magnetic wave.

Since there are many less poles compared to a linear stepper motor, the self-induction is considerably less, which results in a fairly constant force/speed curve that is ideal for motor control (see figure 1.8) [10]. The mass is considerably less, which reduces the total power required and improves the dynamics. Actuation is very smooth, and the motor is only turned on when motion is required, unlike stepper motors where constant attraction is required.

Servomotors require an encoder to know its position or speed. A closed-loop feedback control scheme is required to accurately position the rotor. This adds up to the total cost of such a motor.

All physical features of a linear motor seem to be a prosperous fit to be applied in low-duty CNC machines, except for the price. If outsourced and depending on the motor type, these motors cost minimally 700 euros (company Tecnotion in the Netherlands) per meter stroke, which makes a 3D printer or a laser cutting machine significantly more expensive. The price remains high, even when the model is up- or down-scaled.

1.3 Thesis Proposal & Thesis Outline

The following thesis project is proposed: "The design and manufacturing of a low-cost direct-drive motor, that is specifically optimized for low-duty CNC machines in performance and cost". All physical features of a linear motor seem to be a perfect fit for high-speed manufacturing, except for the cost. To reduce the cost, optimization is performed; manufacturing methods like 3D printing and laser cutting is used; low-cost components and smart design choices are presented to have a fully integrated carriage that is low-cost and performs according to the given specifications.

The thesis is structured in 5 chapters. Following this introduction, an in-depth research regarding linear motors is presented in the chapter 'Introduction to linear motors'. This chapter explains how linear motors physically work; the different motor models that are available today; information regarding encoders; control and commutation methods. The chapter closes with a final motor and encoder choice, that is used to design and manufacture a motor in the follow-up chapter. In this 'Design & optimization' chapter, an analytical model is provided; a finite element model in COMSOL is presented and used for the optimization that is post-processed in MATLAB. The chapter also explains more in-depth regarding the control and commutation implementation. The chapter closes with a CAD motor model. In the next chapter, the experimental set-up is presented and the motor is validated. The results are analyzed and checked whether these fit the requirements. The final chapter will discusses the findings and concludes the report.

Aside to this thesis report, a confidential company report is provided that lists sensitive company information, e.g. final dimensions; code etc. These appendices are in the form 'Appendix C#'.

Chapter 2

Introduction To Linear Motors

2.1 Introduction

In this chapter an introduction to linear motor is given that should help the engineer to get a solid basic understanding on what is required to design a low-cost non-complex linear motor. First the basic physical principle and workings of a linear motor is explained, based on the Lorentz actuator and Lorentz force. Then different linear motor types are presented and related inventions are discussed. Information regarding cogging is given, and methods on how to reduce this effect. Commutation and its different methods, which is the switching of currents to achieve motion, is discussed in the follow-up paragraph. Then a variety of encoders are discussed, that are required for proper commutation and closed-loop position control. Finally, a motor and encoder choice is provided in the final concluding paragraph.

2.2 Physical Principle

A linear motor is very similar to that of a synchronous servo motor. When a servo motor is laid flat and unrolled as can be seen in figure 1.7, a linear motor is realized [65]. The stator that contains the windings in a servo motor, becomes the moving part of the linear motor. The rotor of the servo motor that contains the permanent magnets, becomes the stator of the linear motor. By changing the current phase in the coils of the linear motor, the polarity of each coil is changed. The attractive and repelling forces (based on the Lorentz force) between the electromagnetic coils in the rotor and the permanent magnets in the stator cause the rotor to move and generate a linear force.

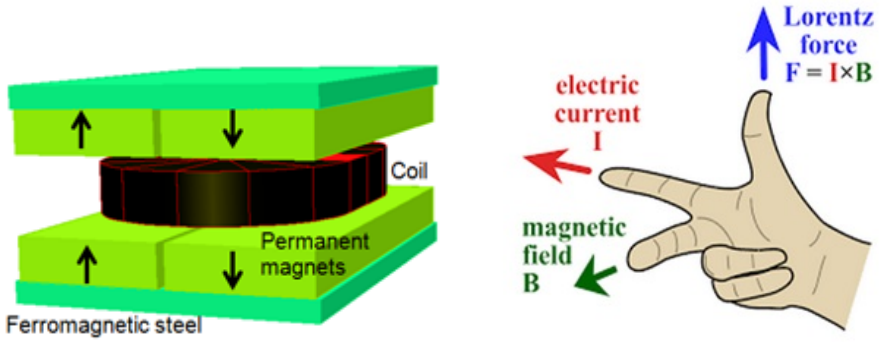

(a) **(b)**

Figure 2.1:
(a) Lorentz actuator. An energized coil is positioned in the magnetic field. The direction of acceleration is determined by the right hand rule (figure 2.1b) [56].
(b) Right hand rule to determine the Lorentz force.

Imagine a simple Lorentz actuator as shown in figure 2.1a. An electromagnetic coil with n windings is positioned in a magnetic gap with flux $\boldsymbol{B}$. Each winding that is placed in the magnetic field has an effective length l_w. If current $\boldsymbol{I}$ flows through the effective length of the coil, an instantaneous Lorentz Force is present that accelerates the coil in a given direction. This force scales linearly with the current. The direction in the case of a non-orthogonal set-up is determined by using the right hand rule as shown in figure 2.1b. The Lorentz force can then be calculated using the (simplified) formula 2.1:

$$\boldsymbol{F} = n\boldsymbol{I}l_w \times \boldsymbol{B} \tag{2.1}$$

A more complex analytical model of the eventually chosen motor type is presented in section 3.3.

Whenever the coil of the Lorentz actuator leaves the magnetic field, the output force is reduced and eventually drops to zero. A solution would be to place multiple magnets of changing polarity after one another, such that with proper switching of the coil current, somewhat continuous acceleration can be achieved. The smoothness of motion and how constant the motor constant is, depends on the number of coils, which directly relate to the number of rotor poles. The number of poles differ from 2 to 8, however the most common set-up is a 3-pole motor. More poles allow for smooth actuation at low speeds, however with fewer poles a more constant force/speed curve is realized, due to reduced self-induction as explained in the general introduction [10]. An extension on the previously described Lorentz actuator is presented in figure 2.2.

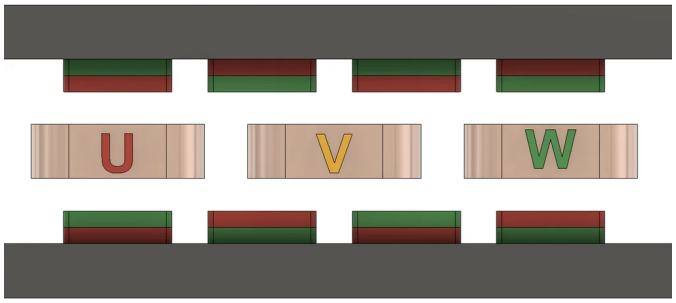

Figure 2.2: A representation of a linear motor, which is essentially an extended Lorentz actuator [63]

A plurarity of the stator pitch (magnetic north to north) is equal to that of the rotor pitch (coil center of phase U to phase W in figure 2.2). The permanent magnets are of changing polarity to create a static magnetic wave with a periodicity, of whose multiple is equal to the length of the rotor pitch. The rotor, in case of three phase motor, contains 3 poles with coils that are positioned such that the three poles (phases) are 120 electrical degrees apart from one another. The full electrical cycle is of the same length as the magnetic cycle. By switching the current of the coils at the right time, one could 'ride' the magnetic wave that is created by the permanent magnets of stator track due to the Lorentz force. More regarding the switching of the currents, commutation, is explained in section 2.5.

Since the motor does not provide positional feed-back, and since the pole pitch is too large, high-precision positioning can only be achieved by using closed-loop position control. A sensor that provides position and/or velocity feed-back is required. Such a sensor is called an encoder. The encoder is used for feed-back position control, but also for Field Oriented Control. Field Oriented Control is used to assure the current vector is 90 electrical degrees off the magnetic field vector to maximize the output force. More information regarding encoders is explained in section 2.6 and more regarding Field Oriented Control is given in section 2.5.4.

In the next section, different linear motor types and their pros and cons are discussed.

2.3 Linear Motor Types

There are a variety of linear motor available. In this paragraph the following motor types are discussed: Flat motor; U-Channel motor; Tubular motor; Induction motor and the planar motor.

2.3.1 Flat Motor

Flat motors are the lowest cost compared to the other varieties. The stator consists of a single track of permanent magnets of changing polarity. Furthermore, the track is backed by iron or a different material of high magnetic permeability to increase its magnetic field strength. As for the rotor, there are two variant: slotted flat motors and slotless flat motors.

Slotted flat (iron-core) motors

The rotor consists of electromagnetic coils that are wound around slots that are of high magnetic permeability. For a high number of slots, and thus poles, the motor could also be used as a

variable reluctance (stepper) motor.

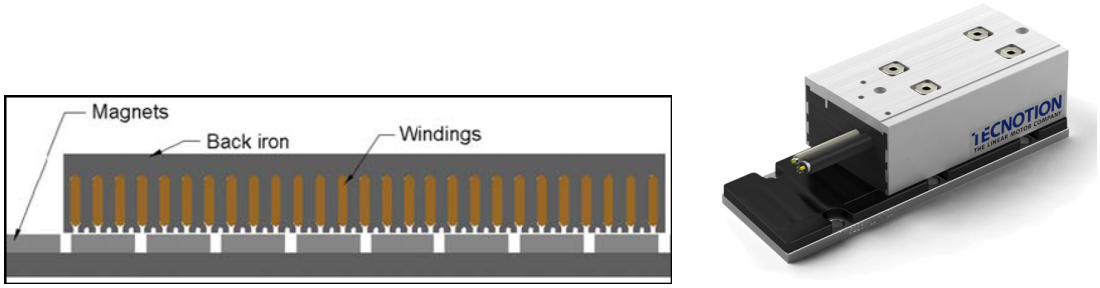

(a) **(b)**

Figure 2.3:
(a) Schematic of an iron-core motor. The primary contains iron backing; iron slots and the electromagnetic coils. The stator contains the permanent magnets.
(b) Tecnotion iron-core motor.

Since iron is also used as backing in the rotor due to its high magnetic permeability, this variant of a linear motor is the heaviest variant of all linear motors (excluding the Induction motor). The magnetic field strength is increased, resulting in strong attractive forces between the stator and rotor that is 5 to 13 times the thrust [52]. This results in a strong preload the engineer has to account for by opting for the correct bearing. These attractive forces result in favorable positions of the rotor compared to the stator, which causes velocity ripples. These attractive forces are called cogging. There are methods to reduce this, and these will be explained in sectopm 2.4.

Since the magnetic field strength is increased due to material of high magnetic permeability, the motor stiffness is significantly higher than other linear motors. The force/volume output is over 125 times larger compared to that of a U-channel motor [52]. Since iron is also great heat conductor, and because of the motor's sufficient surface area, the heat dissipation is efficient.

Slotless flat motors

Slotless flat motors do not have slots in the rotor and come in two variants. Those with iron backing and those without [38].

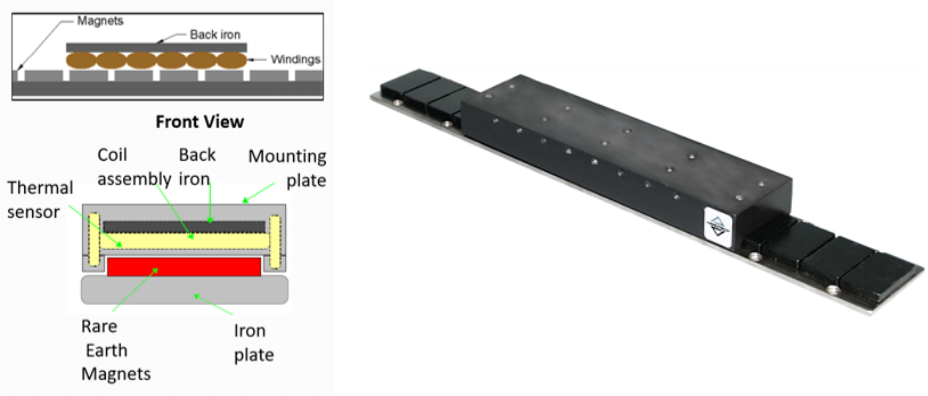

(a) **(b)**

Figure 2.4:
(a) Schematic of a slotless flat motor with iron backing. The primary contains only the electromagnetic coils and iron backing. The stator contains the permanent magnets [52].
(b) Aerotech BLMF series ironless motor. This motor uses no iron backing, noticeable due to the magnets not being skewed to reduce cogging.

With iron backing the heat dissipation is better and the motor's stiffness is increased compared to without, however similar to slotted flat motors attractive forces (cogging) are present. These forces are however lower compared to the slotted flat motor, since the iron backing is at a further distance away from the stator track that contains the permanent magnets. This reluctance force scales with $\frac{1}{airgap^2}$.

Without iron backing, no cogging is present, and very smooth actuation is possible. Since no iron or material with high magnetic permeability is present, large magnetic flux leakage results in reduced motor stiffness. This makes the motor less efficient, and should be compensated by feeding higher current, which results in high heat due to joule heating ($P = I^2R$).

An in-depth patent search has been performed, see figure 2.5. Patent US6522035B1 [57] shows a linear reluctance motor that has 3 poles, where 2 poles are magnetically coupled together to increase its performance.

Patent US5854521A [44] shows a design that could be used both for linear reluctance motors and linear iron-core motors. Instead of having multiple coil in the longitudinal direction, in this design its opted for having these coils in the transverse direction.

2.3.2 U-channel Motor

U-Channel motors are very similar to that of the slotless flat motors. Where a slotless flat motor has a stator with a single track of permanent magnets with iron backing, a U-channel motor has a second track to reduce flux leakage as shown in figure 2.6a. These tracks are connected with one another to realize an efficient flux path, that results in the typical U-shape (see figure 2.6b). This increases motor's efficiency and performance, however comes at an increase of cost.

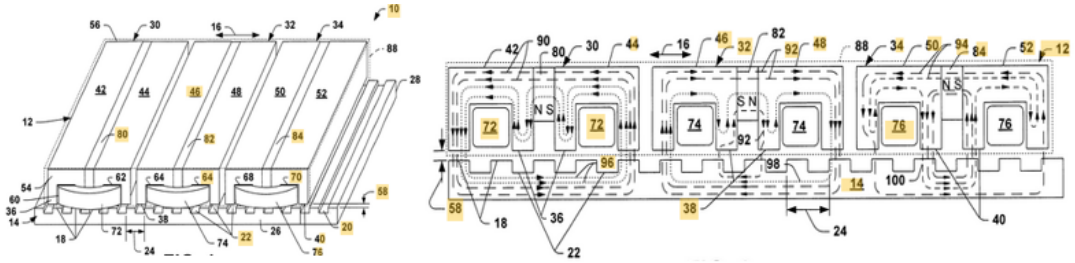

(a)

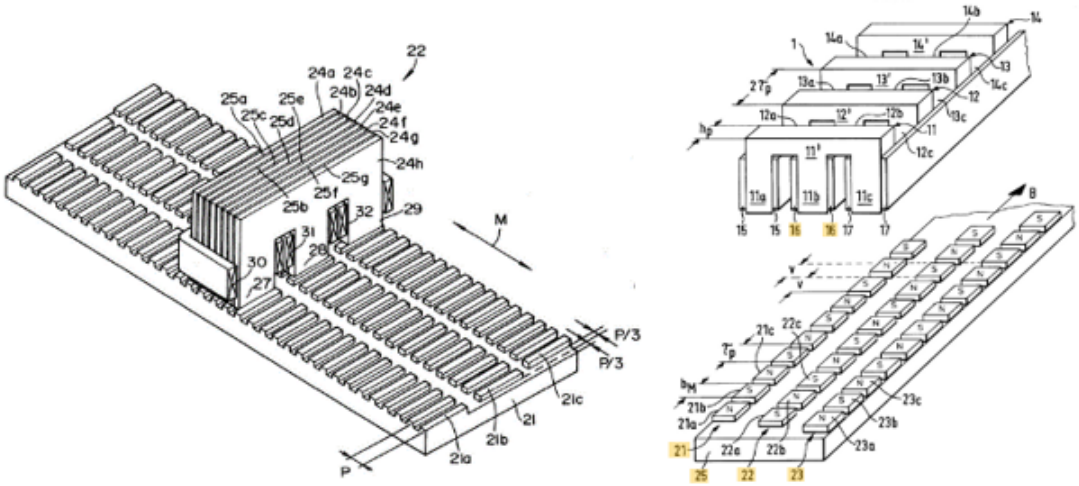

(b)

Figure 2.5:
(a) Patent US6522035B1: Forcer and associated three phase linear motor system (coupled poles) [57].
(b) Patent US5854521A: Multi-phase transverse magnetic flux machine [44].

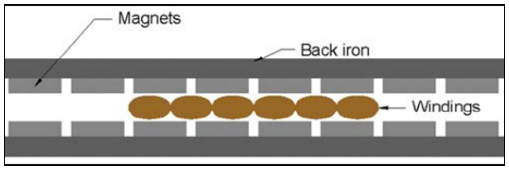

(a)

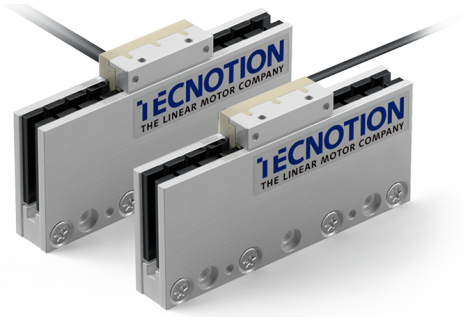

(b)

Figure 2.6:
(a) Schematic of an U-channel motor [52].
(b) Tecnotion U-channel motor. The opposing stator tracks are connected with one another to reduce on flux leakage.

Since the rotor is ironless, no attractive forces or cogging is present, allowing for very smooth control. The rotor is very light, which allows for very fast movements. The design is airgap forgiving, since the amount of flux leakage is considerably less compared to the flat motors due to the opposing permanent magnets [38].

The rotor is positioned between the stator tracks, which means that little surface area can dissipate the heat. Without cooling, these motors are very limited in current input and motor force output. For this reason, water cooling is often used to dissipate the heat, especially in vacuum applications [52].

Patent US6919654B2 [23] shows a design where the magnetic track is instead surrounded by the rotor coils with iron slots and backing. This reduces the amount of bending of the magnetic track compared to the conventional U-channel motor. Furthermore, since this design uses iron in the rotor, cogging is reduced by skewing the slots (more in paragraph X).

Patent US6239516B1 (expired) [21] shows a design where the coils can be stamped, etched or deposited and adhered to a rigid substrate. The advantage here is a significant reduction in cost and the ability to create complex windings for improved performance. Also, since the windings are compact, the airgap is reduced and thus increases performance.

Patent JP2011193553A [66] shows a 2-DOF design that allows for longitudinal motion and transverse motion. This may be interesting for 3-DOF gantry designs to reduce the amount of actuators.

Since heat is a significant issue for U-channel motors, patent KR100726533B1 [67] introduces a cooling method that reduces thermal deformation. The design is of small size, high rigidity and high reliability.

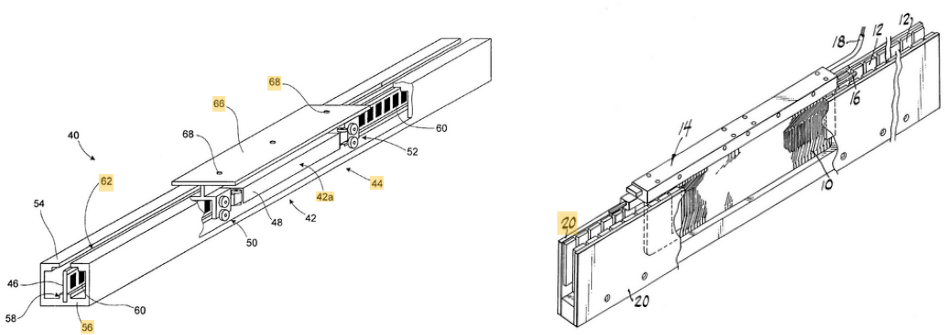

(a) **(b)**

Figure 2.7:
(a) Patent US6919654B2: A design which counters the bending of the stator tracks [23].
(b) Patent US6239516B1: The ability to create complex windings [21].

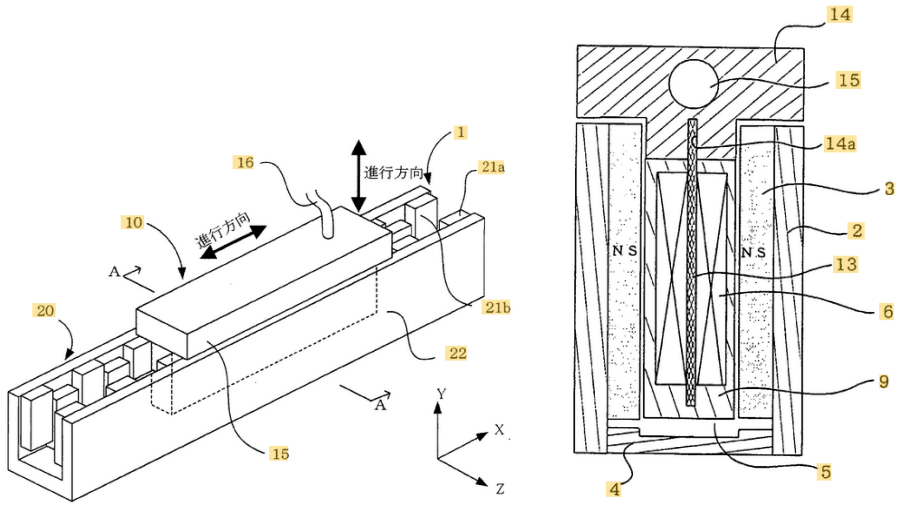

(a) (b)

Figure 2.8:
(a) Patent JP2011193553A: 2-DOF U-channel motor [66].
(b) Patent KR100726533B1: Cooling method using a heat pipe to increase heat dissipation [67].

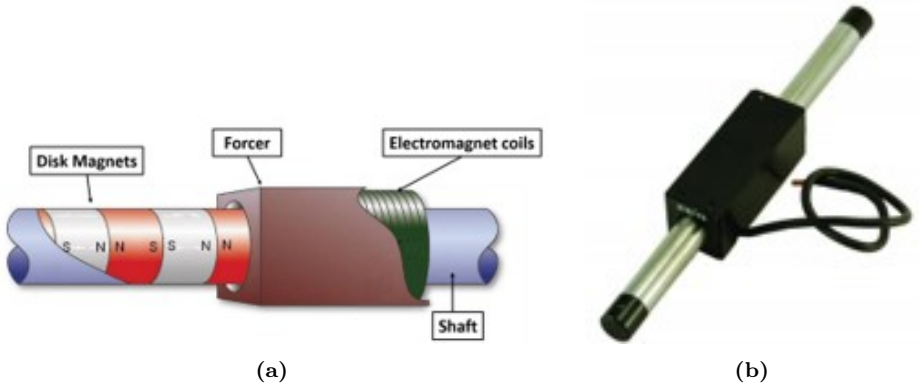

(a) (b)

Figure 2.9:
(a) Schematic of a tubular linear motor. The rotor surrounds the stator, effectively using all flux [47].
(b) Nippon Pulse tubular linear motor [47].

2.3.3 Tubular Linear Motor

The tubular linear motor consists of a stator that is tubular in shape, in which magnets of changing polarity are positioned, with or without spacers. The rotor consists of coils with or without iron slots and with or without iron backing. The tubular linear motor is a very efficient motor, since the rotor's coil surround the magnets and uses all the magnetic flux from the stator. Since the stator is well surrounded, the air-gap is non-critical and may vary from 0.5 [mm] to 2.5 [mm] [38] [52] [64] [47].

In the case of using iron in the rotor, one has to account for the attractive forces (cogging). For this motor, in order to reduce these, one should change the magnet orientation from longitudinal to transverse, or by using radial magnets. One cannot skew the magnets in an original tubular linear motor, nor change the angle of the iron slots or iron backing. The only two effective methods are to correct using a control scheme, or use more teeth in the rotor than there are magnets in the stator's magnet pitch to create destructive interference (see cogging section 2.4).

Without iron, these motors have a very wide speed range from several $\mu m/s$ to over 10 m/s, with very smooth control [47]. These motors may be applied in a large variety of applications. The motor stiffness is approximately a 100 times the U-Channel's motor stiffness, which can compete with iron-core flat motors. The heat dissipation is however over 4 times better than those of flat motors since the heat can dissipate in all directions [52].

Different designs can be found in the state-of-the-art. Patent JP4860222B2 [28] shows a design where adjacent coils are connected using resin spacers, and inserted in a holder that makes wiring easier.

Patent US7752736B2 [48] shows a method to create a stator of alternating poles using electromagnetic coils intended for tubular stepper motors. The patent also provides a fixture for the magnetizing coils.

Patent US6313552B1 [8] shows a design that tackles bending of the stator due to its own and rotor's mass for longer axes. This has implications on the rotor design, since the coils have to wound differently, possibly increasing motor cost.

Patent US9379599B2 [59] shows a stator design, in which permanent magnets are interposed with spacers that are of high magnetic permeability. Using these spacers increases thrust, since the flux path is made more efficiently. Furthermore, the design reduces the attractive forces by increasing the magnetic gap for the teeth, around which the coils are wound.

Patent KR101018521B1 [60] shows a stator whose surface area is increased in order to allow for larger (custom) magnets, that increases motor performance.

Patent EP0878899A1 [33] shows a stator that uses ring magnets, that are tightened together using a long screw. The screw may be of soft magnetic material, to increase efficiency.

Patent US6313551B1 [24] shows a tubular stator design that uses a Halbach array, to increase the magnetic field flux. A Halbach array is a special arrangement of permanent magnets that augments the magnetic field on one side, while cancelling the magnetic field to near zero on the other side [34]. This effectively increases motor performance, however for this type of motor requires special magnets.

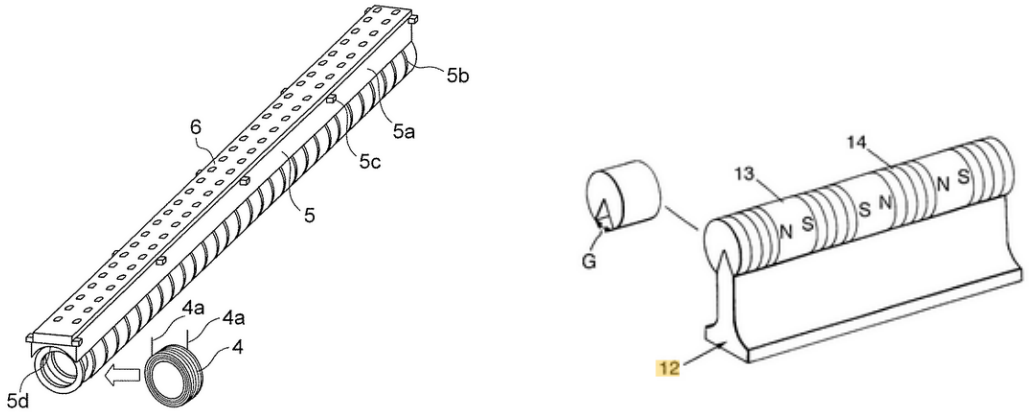

(a) **(b)**

Figure 2.10:
(a) Patent JP4860222B2 [28]: Special coilholder using resin spacers.
(b) Patent US6313552B1: Increasing the stiffness of the stator [8].

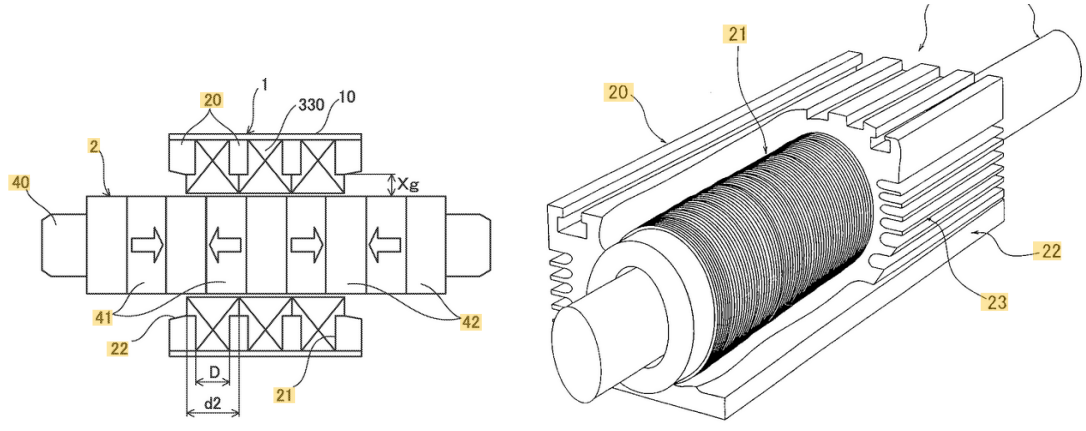

(a) **(b)**

Figure 2.11:
(a) Patent US9379599B2: Uses spacers of high magnetic permeability in order to increase motor performance [59].
(b) Patent KR101018521B1: Cooling method using a heat pipe to increase heat dissipation [60].

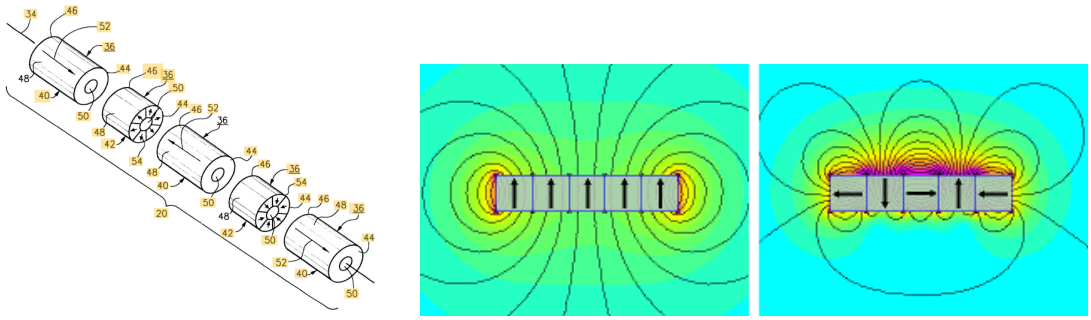

(a) (b)

Figure 2.12:
(a) Patent US6313551B1: Halbach array incorporated in a tubular linear motor [24].
(b) Halbach array: Augments the magnetic field of the stator on the rotor's side [34].

2.3.4 Inductive Linear Motor

The inductive linear motor is an asynchronous motor. The motor runs at a speed that is lower than that of the synchronous speed. The motor does not contain permanent magnets, but instead operates due to Lenz law. The stator consists of coils with an iron-core and iron backing, whereas the rotor consists of an aluminium sheet with iron backing [18].

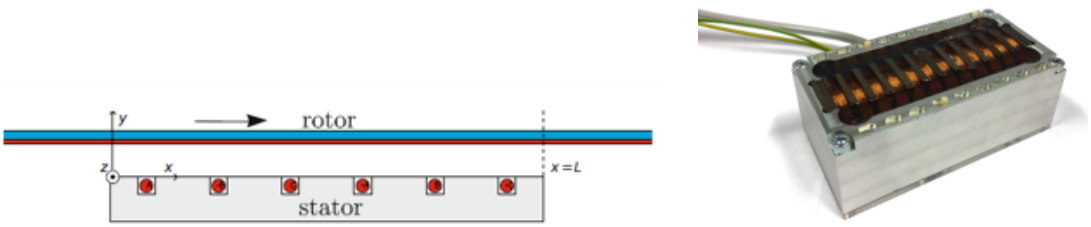

(a) (b)

Figure 2.13:
(a) Schematic of a linear induction motor (SLIM) [53].
(b) The stator of a linear induction motor. [53]

By introducing a changing magnetic field using the electromagnetic coils of the stator, eddy currents are induced in the aluminium sheet, which in turn introduce their own (weaker) magnetic fields that opposes the initial magnetic field. The effect is called Lenz law and the result is thrust.

However, for the linear variant, static and dynamic end effects of the rotor reduce the efficiency significantly [53]. Static end effects are due to large flux leakage at the stator's ends and the dynamic end effects are due to the rotor being magnetized and demagnetized when moved and becomes more troublesome at higher speeds. The static end effects are reduced by using iron backing. These end effects are not present for the rotary variant, which significantly increases the efficiency for the rotary variant.

Furthermore, since the stator contains much iron and windings to compensate for the low efficiency, this type of motor is the heaviest variant of all linear motors. One method to increase the efficiency is to add another stator on the other side of the rotor, turning this motor from a single sided linear induction motor (SLIM) into a dual sided linear induction motor (DLIM). Furthermore by using a DLIM configuration, attractive forces between the stator and rotor are cancelled.

Patent EP1330864B1 [37] shows the design of a 2 axis positioning system that uses linear induction motors. By changing the polarity of the electromagnetic coils, the soft iron is magnetized, and depending on the geometry creates a magnetic field in a certain direction as can be seen in figure 2.14. This design reduces flux leakage significantly, however dynamic end effects are still present.

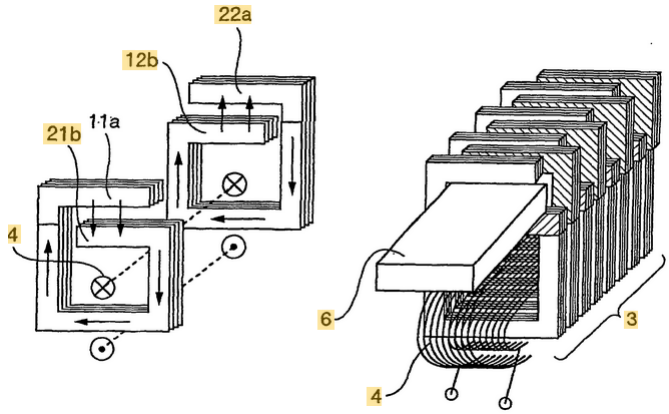

Figure 2.14: Patent EP1330864B1: Linear induction motor design with a small airgap intended for a 2-DOF gantry [63]

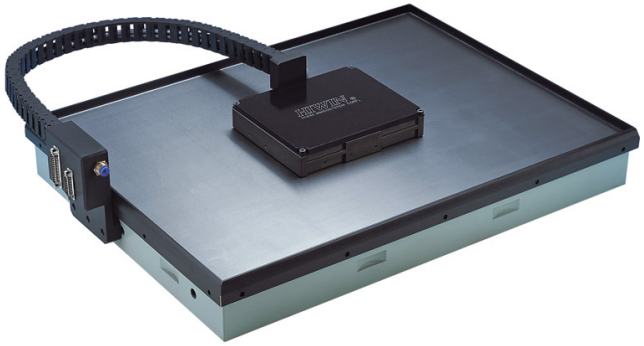

Figure 2.15: A Hiwin planar linear motor. The design incorporates an air bearing.

2.3.5 Planar Linear Motor

Planar motors (see figure 4.1) are a variant on the flat motors, however extended such that up to 6-DOF positioning can be achieved. The motor consists of a rotor and stator that are an array of permanent or electromagnetic magnets, whose choice may depend on the design requirements.

For 6-DOF positioning, an air bearing is used. In the case of using permanent magnets for the stator, a Halbach array is preferred to augment the magnetic field at the rotor's side.

Planar motors have a large variety of applications and may be used in any orientation. A thorough patent search shows different designs for the planar linear motor. Due to the complexity of this type of motor, this introduction is only meant to inform and is mentioned for completeness.

Patent USRE41232E1 [26] shows a 6-DOF planar motor with different coil orientations that are controlled differently.

Patent US6452292B1 [5] shows a planar motor whose stator consists of a coil array, where the first coil array has a plurality of polygonal shaped coils extending longitudinally in a first direction, and a second linear orthogonal coil array having a plurality of oval shaped coils extending longitudinally in the second direction.

Patent US6445093B1 [6] gives different planar motor designs, where the stator may be an array of electromagnetic coils or permanent magnets. The patent also gives a rotor design made from permanent magnets in the case of using a stator that only contains electromagnetic coils.

Patents US6285097B1 [25] and US6188147B1 [27] show different designs for the stator, in which a Halbach array is included to augment the stator's magnetic field at the rotor's side by using transverse permanent magnets. The permanent magnets may be positioned in a checkerboard manner, or diagonally as can be seen in figure 2.16b.

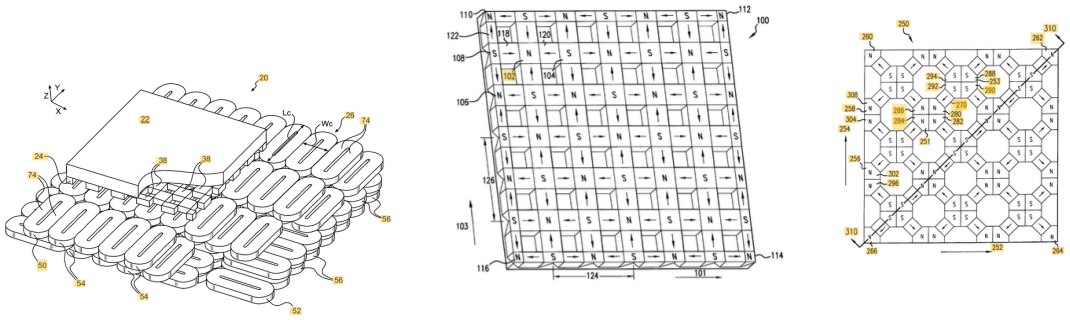

(a) **(b)**

Figure 2.16:
(a) Patent US6445093B1: In this particular design the rotor consist of permanent magnets, wheras the stator consists of electromagnetic coils [6].
(b) Patent US6188147B1: Planar motor stator with Halbach array to augment the magnetic field on the rotor's side. Left: checkerboard array, Right: Diagonal array [27].

2.4 Cogging

Using iron or material of high magnetic permeability in the rotor often results in more thrust, since the amount of flux leakage is reduced significantly. However including material of high magnetic permeability comes with an issue that has to be overcome.

Cogging is the undesirable effect of some permanent magnet motors where varying attractive forces between the rotor and the stator cause force and velocity ripple along the axis [16]. This is the case when the rotor includes material of high magnetic permeability. For stepper motors cogging is also known as 'no current' force/torque [42]. The effect is especially significant at low speeds, since at higher speeds the motor's inertia helps smoothen the force ripple. The attractive forces scale with distance as $\frac{1}{airgap^2}$.

As the rotor travels along the axis, the rotor has preferable positions relative to the permanent magnets. In order to overcome these attractive forces, more force is required. This force variation causes the velocity ripple, which reduces the smoothness of travel. For that reason, when smooth motion, or constant force/velocity is required, an ironless motor is preferred [16].

There are options to reduce these cogging forces, however these come at a cost of efficiency. One could skew the magnets or change the magnet's shape (see figure 2.17a), to smoothen the velocity ripple. Another option is to skew the iron slots/backing in the linear motor, which essentially does the same.

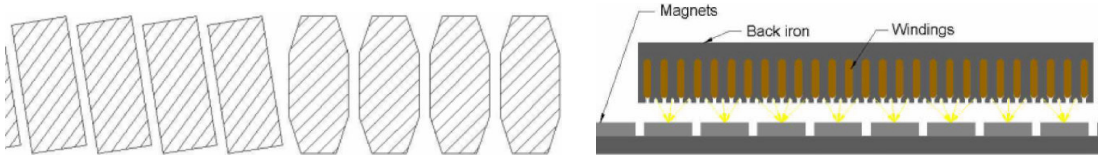

(a) (b)

Figure 2.17:
(a) Cogging: change the magnet's shape or orientation to reduce cogging [16].
(b) Cogging: use destructive interference to reduce cogging. Inner teeth cancel the attractive forces [16].

Another option, in the case of iron-core motors (those that use slots), is to use destructive interference to effectively reduce the cogging forces (see figure 2.17b). In this design there are more slots in the rotor than there are magnets in the stator. This results in attractive forces that cancel one another for the inner teeth. Only the strong preload is still present. In order to cancel the attractive forces for the outermost teeth, a triangular component is added to the lamination ends, which changes the shape of the lamination (from rectangular to a parallelogram), which produces a cogging force that is equal but of opposite to that of lamination.

Another option would be to compensate using control software. The currents are changed such that force and velocity ripple is minimized. These control algorithms can help iron-core motors achieve motion that rivals ironless motors in smoothness and consistency [16].

Implementing anti-cogging methods increases the overall complexity of the motor, which generally results in higher cost, but can provide higher force output.

2.5 Commutation

Commutation is the process of switching currents of the coils in order to achieve motion [7]. As the rotor moves along the axis, the coils are energized such that the rotor is being pulled and

pushed to the next position. In order to achieve maximum efficiency, it's important to know where the motor is located compared to the stator's magnetic field to energize the coils with the right amplitude and polarity. Hall sensor's are most often used to determine the rotor's position in the magnetic field, however encoders may do the same [35]. Control algorithms (indirect Field Oriented Control) that measure the back EMF can also estimate the position in the electromagnetic cycle.

There are three methods of commutation for three phase motors (see figure 2.18), namely: trapezoidal commutation; modified six-step commutation and sinusoidal commutation. With every change the input currents represent more of a sinusoidal shape, increasing the smoothness of the actuator. For that reason most linear motors use sinusoidal commutation, however increases the complexity of the control algorithm and thus increases cost.

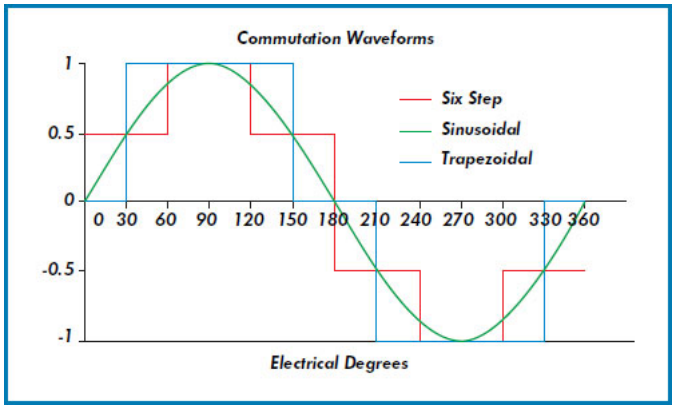

Figure 2.18: The different methods of commutation: Trapezoidal; Six-step and sinusoidal. [7]

2.5.1 Trapezodial Commutation

Trapezoidal commutation is the cheapest variant. The commutation requires hall sensors that are placed 30 electrical degrees from the phase's zero crossing point and 120 electrical degrees apart [7]. Whenever there's a transition in the hall sensors, the currents are switched and commutation occurs. Trapezoidal commutation is often referred to as six-step commutation, since the hall sensors provide 6 different states every 60 electrical degrees. Since the currents are switched in a DC manner, which is not a great fit to the sinusoidal magnetic field of the stator, disturbance forces are introduced causing unsmooth motion. Furthermore the running temperature and power use of the motor is higher than the other alternatives, since the currents are not switched efficiently [17].

2.5.2 Modified Six-step Commutation

Modified six-step commutation is an extension to the trapezoidal commutation, however requires an additional current sensor to sense two different levels of the hall sensors [7]. This results in commutation that looks more like sinusoidal commutation. The disturbances are reduced, increasing the smoothness, however are still present. The running temperature and required power is lower than that of trapezoidal commutation, however higher than sinusoidal commutation. This method is slightly more expensive than trapezoidal commutation since an additional current sensor is required.

2.5.3 Sinusoidal Commutation

The ideal type of commutation that minimizes the disturbances; the total power usage and allows for smooth actuation, is sinusoidal commutation [17]. The sinusoidal currents are 90 electrical degrees offset to the magnetic field, which results in a fairly constant Lorentz force. This method however requires an accurate estimation of the rotor's position compared to the stator's magnetic field.

There are two methods to estimate the position in the electrical cycle. The first and cheapest option is to use analog hall sensors that output a sinusoidal signal that represents that stator's magnetic field [7]. These signals are then combined with a demand signal to correctly commutate the rotor. However, hall sensor may pick up noise, which may affect the smoothness of the commutation.

Another more popular method is to use an encoder to estimate the rotor's position. This brings a higher level of accuracy for commutation, resulting in smooth motion with faster settling times and tighter servo loops [7]. Since most linear motors are used in closed-loop mode, and positional data is available, it's a no-brainer to implement this method.

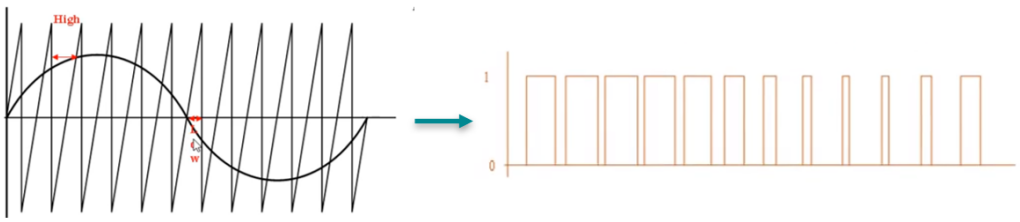

Figure 2.19: Sine Pulse Width Modulation: a carrier signal is used to convert the sine to PWM. [61]

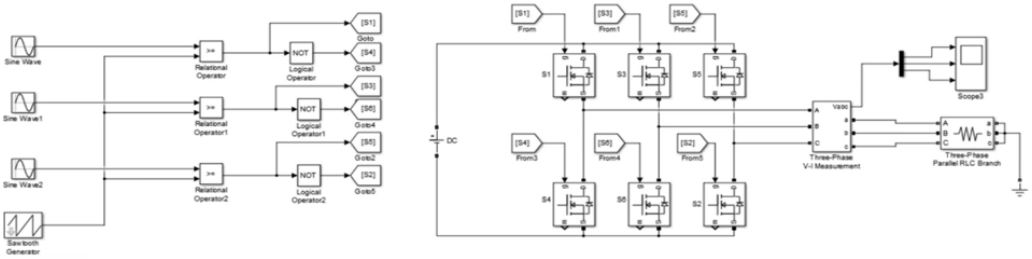

Figure 2.20: Simulink model of SPWM. The compared signals are fed to the tripple H-bridge.[61]

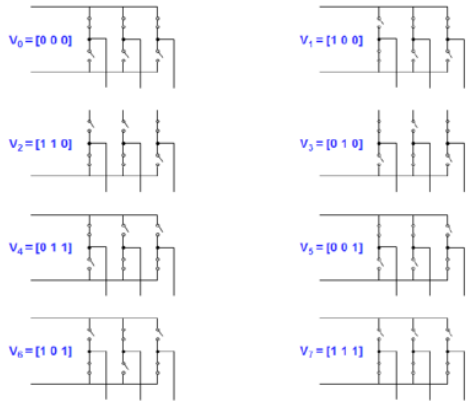

Figure 2.21: The tripple H-bridge allows for 8 different states, of which V0 and V7 are the zero current states. [45]

There are two methods of sinusoidal commutation, where Pulse Width Modulation is used with a triple H-bridge to create a sinusoidal signal, namely Sinusoidal Pulse Width Modulation (SPWM) and State Vector Pulse Width Modulation (SVPWM). SPWM [61] is the process where a sinusoidal signal is compared to a sawtooth waveform, that is of the same frequency of the required PWM signal (see figure 2.19). Whenever the sinusoid is above the sawtooth, the PWM gives a high and whenever the sinusoid is below it gives a low. These signals are then fed to the triple H-bridge to create the three phase signal by switching between 8 different current vectors (see figure 2.20 and 2.21). The triple H-bridge consists of 6 MOSFETs that are coupled in pairs. Vectors V0 and V7 are known as the zero current vectors, since no current flows through the motor (Kirchhoff's law). The amplitude of the sawtooth waveform represent the maximum magnitude of the signal that is fed to the motor. The maximum peak voltage using this algorithm is 0.5 * supply voltage.

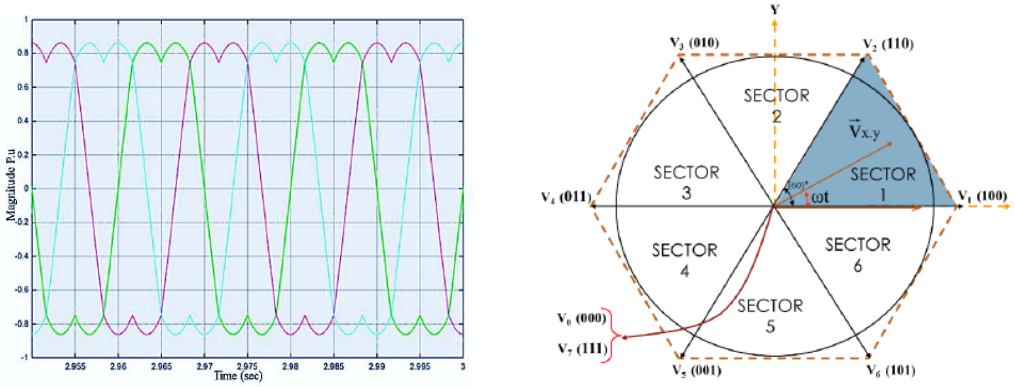

(a) **(b)**

Figure 2.22:
(a) The output current waveform of the three phases when using SVPWM. [1].
(b) SVPWM: 6 different sectors. The total current vector can be formed by 2 non-zero current vectors and one zero current vector. [1]

In order to increase the maximum peak voltage, SVPWM [45] [1] can be implemented in the control algorithm. Instead of comparing the sinusoidal signals with a saw-tooth function, one calculates the switching times of the triple H-bridge current vectors, such that the magnitude and direction of the total phase's current vector can be manipulated. This results in a different looking output waveform that looks like figure 2.22a, however if the inductance of the coils is large enough, the waveform smoothens to a sinusoidal waveform that has a peak voltage that is of larger magnitude compared to that of SPWM. The maximum peak voltage is $\frac{1}{sqrt(3)}$ * supply voltage, which is a 15 percent increase over SPWM.

The electrical cycle is divided in 6 different sectors. The position in the electrical cycle provides information regarding what sector is selected. Each sector uses three triple half-bridge current vectors to create a current vector of a certain magnitude in a certain direction, namely a zero current vector (V0 or V7) and two non-zero current vectors (see figure 2.22b). The switching times are then calculated and are different for each sector. These calculations are shown in Appendix 6.1. A representation of the SVPWM algorithm is given in Appendix 6.2 and implemented in Simulink in section 3.6.

Using SVPWM does require more (significant) computational power compared to SPWM. For that reason a look-up table is preferred to avoid delays in the control loop.

2.5.4 Field Oriented Control

In order to achieve maximum efficiency during commutation, it's required that the current vectors of the coils are 90 electrical degrees offset to the magnetic field (right hand rule Lorentz force) [51]. At increasing speeds, the phase currents may have a phase lag compared to the input potential due to the inductance of the motor coils (see figures 2.23 and 2.24). This results in the current vector being no longer orthogonal to the magnetic field, resulting in reduced motor performance.

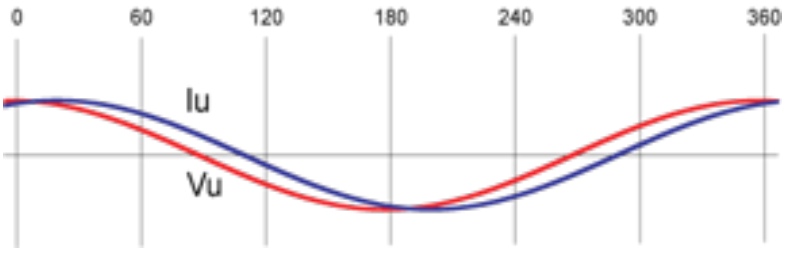

Figure 2.23: At increasing speeds, due to the inductance of the coils, the current lags behind the potential.[51]

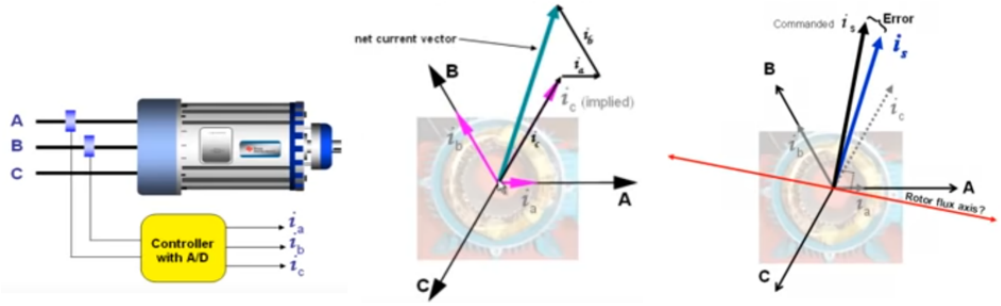

Figure 2.24: At increasing speeds, due to the inductance of the coils, the current lags behind the potential, causing the current vector to be non-orthogonal to the magnetic flux. [32]

In order to account for this effect [32], two current sensors are used to measure the currents. The currents are then controlled with three PI controllers, such that the current vectors are again made orthogonal to the magnetic field. This results in high efficiency over a high velocity range, and results in smooth control, since the motor constant remains constant and no longer degrades at higher speeds. Only two current sensors are used, since the third phase's current may be calculated using Kirchhoff's law. Current that enters two of the motor's phases has to pass through the third phase, since the motor is a closed electrical system. A representation of this set-up is shown in figure 2.24.

The most simplest form of Field Oriented Control is to use three PI controllers that each control the current of a single phase as can be seen in Appendix 6.3. This control scheme may be simplified using Clarke's transform, that changes the reference frame from a three axis (abc) reference frame to a two axis (alfa beta) reference frame. This results in a reduction of control effort, since now only two PI controllers are required to control the 'alfa beta' reference frame. The inverse Clarke transform can then be used to reconstruct the three phase signal.

One could further simplify this control scheme by using the Park's transform. Since the 'alfa beta' reference frame is still AC in nature, high-bandwidth PI controllers are required to effectively track the input signal. By using Park's transform, one can convert a two axis ('alfa beta') reference frame to a rotating two axis 'dq' (direct & quadrature)' reference frame. The result is a DC control signal that can be easily tracked with low control effort. This method however requires rotor's position data to determine the position in the electrical cycle.

This position data can be extracted from an encoder, which is called direct Field Oriented Control. This provides the most accurate results compared to indirect Field Oriented Control [51]. Indirect Field Oriented Control requires an accurate motor model and uses the impedances of the coils (inductance and resistance) [53]. With this motor model the back EMF is estimated and the position in the electrical cycle is determined. This method does not require additional sensors, however results in longer computation time and is not as accurate as direct FOC.

Figure 2.25 shows the Clarke and Park transforms and shows how the signals are modified.

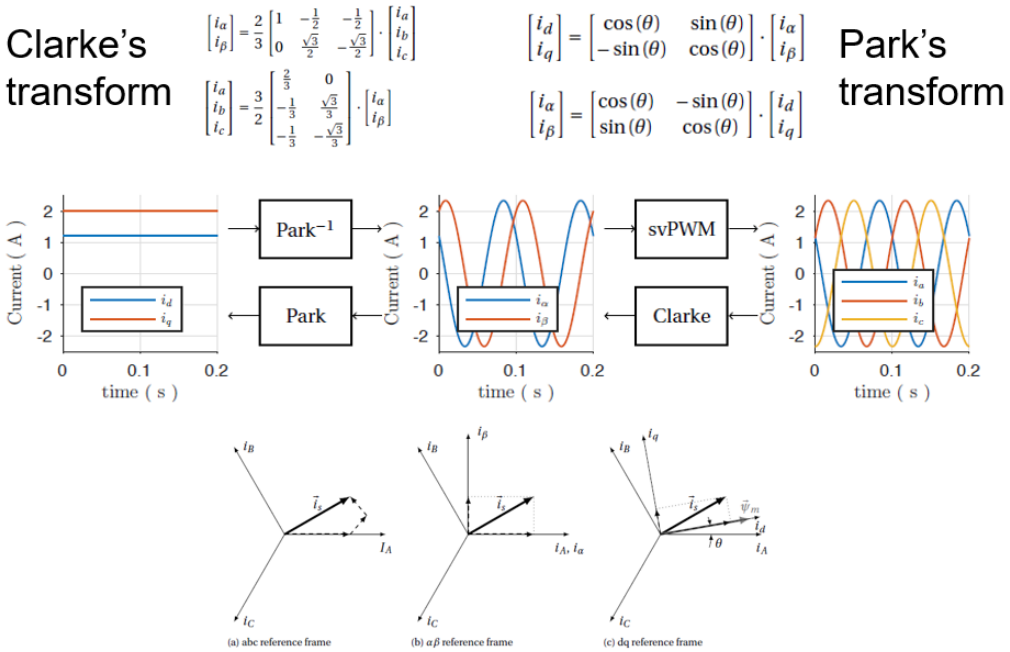

Figure 2.25: Clarke and Park transforms that simplify Field Oriented Control. [53]

2.6 Encoders

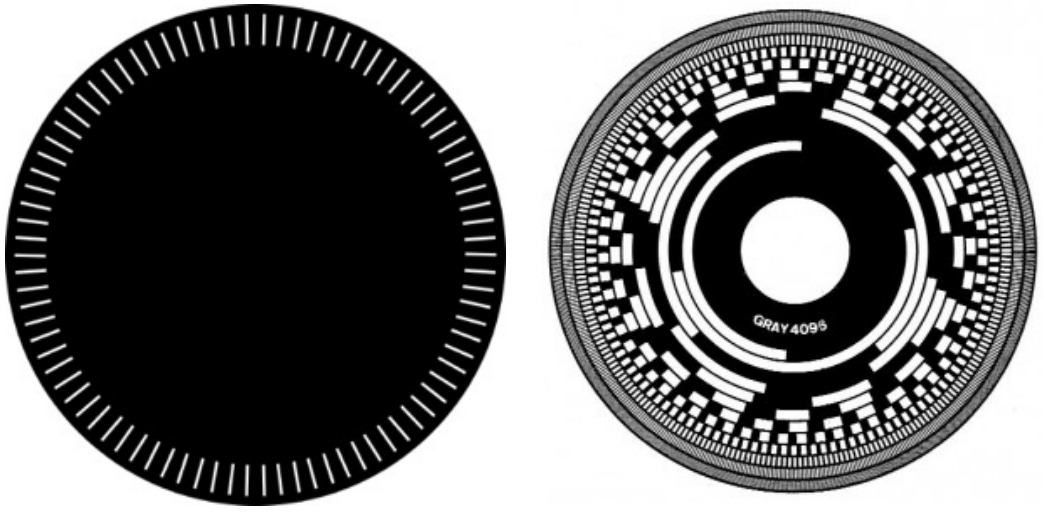

(a) **(b)**

Figure 2.26:
(a) Rotary incremental encoder: the disk contains consistent incremental lines [36].
(b) Rotary absolute encoder: the disk has a unique pattern for each position [36].

2.6.1 Absolute & Incremental Encoders

In order to properly and accurately commutate and control the motor, an encoder is required. An encoder is a sensor that provides positional and/or velocity data. One can differentiate between absolute and incremental position encoders. Absolute position encoders provide direct position data, whereas incremental encoders only provide information about how many 'steps' were made and thus requires a reference point to know its position [36]. In many practical applications for incremental encoders the zero reference position is found using 'homing', where a motor moves to one of its axis's ends and bumps against a sensor, which tells the controller that that is the zero reference point. A sensor is not necessarily required, and homing may be performed using an algorithm or by measuring the back EMF. Since absolute encoders are slightly more advanced, the total cost of these encoders is higher than incremental encoders.

An absolute encoder requires a pattern that is unique for every position (see figure 2.26a). Engineers classify the absolute encoder by the number of output bits, which is directly related to the absolute resolution along the axis [36]. Absolute encoders have the advantage of non-volatile memory. That means that when the power fails, it can still track the position. For that reason absolute encoders are used when safety is of great importance.

An incremental encoder uses a pattern that is periodic, where the features are consistently spaced apart, similarly to a ruler (see figure 2.26b). Two sensors (A and B) are spaced 90 electrical degrees apart, which then output a block signal that is also 90 electrical degrees apart. Depending on which signal leads, the direction and step size is extracted. Incremental encoders can achieve a maximum resolution of 1/4th the pattern pitch. For that reason they're often called quadrature encoders [41].

The encoders can further be classified in analog or digital encoders.

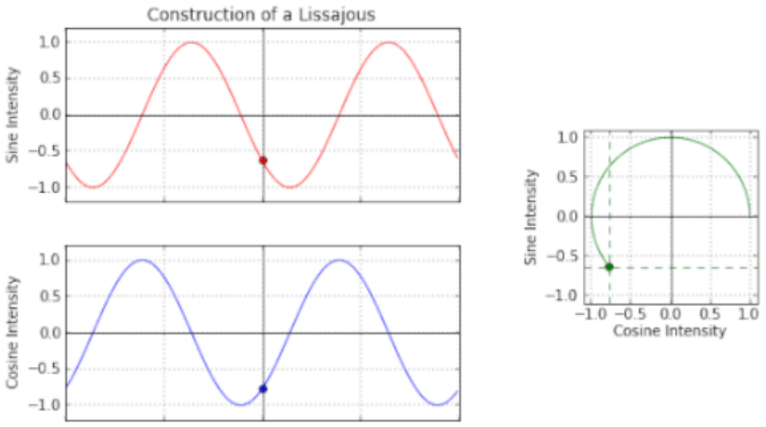

Figure 2.27: A cosine (channel A) and sine (channel B) can form a Lissajous figure from which angular position data may be extracted [15]

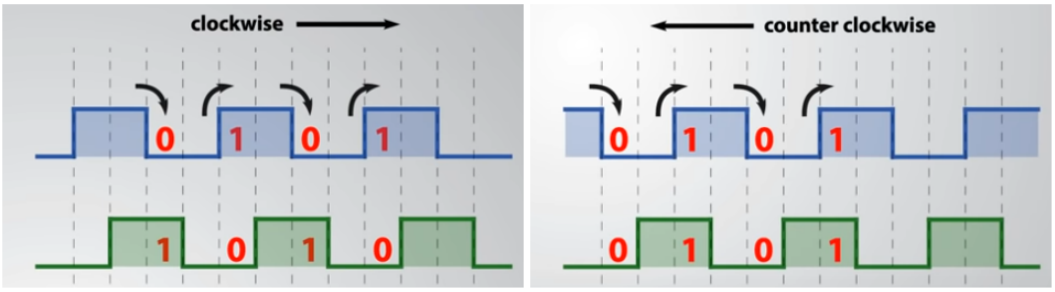

Figure 2.28: An incremental encoder gives direction and step information from channel A & B [41].

2.6.2 Analog & Digital encoders

Analog encoders use sensors that are 90 electrical degrees spaced apart, and readout a continuous signal. Due to the spacing, one channel outputs a cosine whereas the other outputs a sine. By combining these two signals, a Lissajous figure can be constructed from which very fine position (angle) data can be extracted [15]. Analog encoders are however sensitive to errors: signal offset (gain related); signal imbalance and phase error. These can however be countered with different compensation techniques.

Digital encoders do not necessarily rely on a continuous signal, however outputs a digital signal that can be read out fast. These encoders have improved noise immunity and do not require compensation techniques. A noisy analog continuous signal can be converted into a digital signal by using a Schmitt trigger [36]. A Schmitt trigger can convert a noisy signal into a well readable signal as can be seen in figure 2.29.

Different encoders may use different physics in order to determine the position. Optical encoders use (infrared) light; magnetic encoders use electromagnetism; capacitive encoders use electrostatics and inductive sensors use induction to determine the position or velocity data.

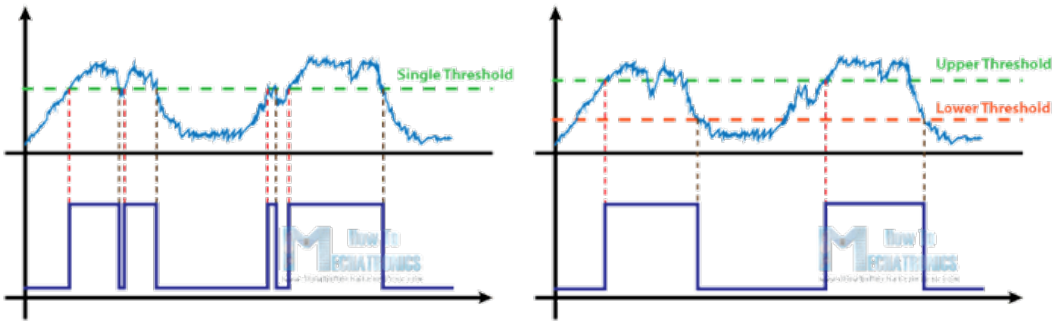

Figure 2.29: A Schmitt trigger improves noise immunity by digitizing an analog signal [36].

2.6.3 Optical Encoders

Optical encoders dominate the industry. They're the most accurate and cost-effective encoders, however are sensitive to contaminations and environmental changes [39]. The sensors used in optical encoders are photoresistors; phototransistors; photodiodes; CCD and CMOS. For very

high precision applications, a clean and dust-free environment is a must. The minimum resolution ranges from hundreds of micrometers to sub-nanometer resolution.

Two advanced methods can improve on encoder resolution for optical encoders: interference and diffraction. Interference in optical encoders work by using a line Moiré pattern, where two patterns with different pitch are moved or rotated over one another. This results in an optical illusion where a small movement can be seen as a large displacement, which can be easily detected. Another great application of line Moiré is the Moiré caliper [22]. Using this caliper it's fairly easy to readout sizes that are under 1 [mm] in size. See figure 2.30a.

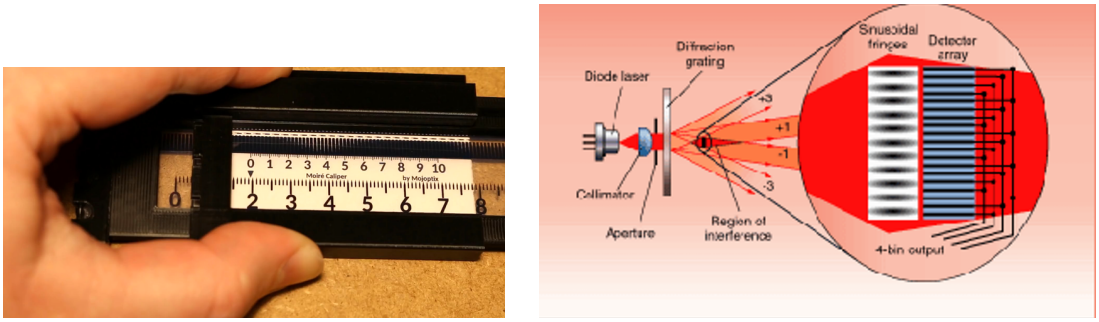

(a) **(b)**

Figure 2.30:
(a) A moiré calipre allows easy read-out of small features [22].
(b) Diffraction optical encoder: shift of diffraction pattern gives position data [29].

Diffraction-based encoders rely on the bending of light. A detector array senses the sinusoidal fringes that are generated by a diffraction grating [29]. The detector detects a shift of the diffraction pattern caused by grating movement. Tracking this shift yields highly accurate position data. A typical diffraction encoder is shown in figure 2.30b.

2.6.4 Magnetic Encoders

Magnetic encoders are the second most popular encoders in the industry. The encoder generally contains hall sensors that measure the magnetic field of the magnetic encoder strip or disk in order to determine its position. However, electromagnetic coils or magneto-resistive sensors may also be used as sensors. The output may be a block signal, or a continuous analog signal.

Figure 2.31: A magnetic encoder that contains a sensor head and magnetic encoder strip [11]

.

For incremental magnetic encoders, an active or passive magnetic scale can be used. The magnetic scales are generally coarser than optical scales, however high resolution of minimally 1 micrometer can be achieved [11]. In order to get nanometer resolution, interpolation is used for analog hall encoders.

Magnetic encoders are more robust than optical encoders, since dust or other contaminations have little effect on the output. However, magnetic encoders are sensitive to electromagnetic interference and should thus be well shielded. Furthermore, high temperature may demagnetize the encoder strip over time and should thus be accounted for.

2.6.5 Capacative Encoders

Capacitance rely on the change in capacitance value of a capacitor to measure displacement. The encoder consists of a transmitter; a rotor and a receiver as can be seen in figure 2.32. A high frequency reference signal passes through the rotor, which contains etched sinusoids. This etched pattern modulates the high frequency signal of the transmitter in a predictable manner [13].

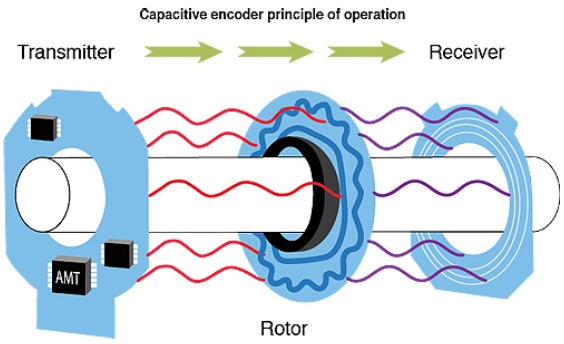

Figure 2.32: A capacative encoder uses high frequency signals to detect a change in capacitance. This change is then converted to position data. [13]

.

The receiver disk reads the modulations and on-board electronics then convert this data to increments which can be used to measure displacement. Capacitive encoders are more robust than optical encoders, however are sensitive to dirt and dust, which reduces the relative permittivity of the rotor [13]. Furthermore, since the method relies on electric fields, the encoder is sensitive to electrical interference and should be well-shielded.

Capacitive encoders can provide better resolution than magnetic encoders, however are generally more costly.

2.6.6 Inductive Encoders

Inductive sensors are uprising in the high-tech precision industry, since the resolution is very high and the encoders are very robust to external factors. An inductive encoder detects a linear displacement or rotation relative to its target. The encoder contains a transmitting coil and four receiver coils (see figure 3.6). An electromagnetic field is transmitted, which is manipulated whenever a conductive material enters the electromagnetic field [55]. The four receiver coils detect this change and is then converted to displacement information.

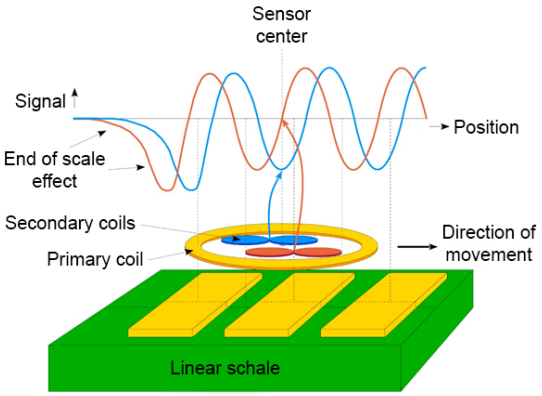

Figure 2.33: An inductive sensor is very robust due to the receiver coils being able to filter external interference. [55]

.

A 'stator' track containing copper markings over which the encoder moves. The copper markings are about two thirds in width, and have gap of one third. Together, these dimensions make up the pitch period of the inductive encoder. Whenever there's motion, the output signal is a cosine and a sine, which is then digitized to a square wave (analog encoders using a Schmitt trigger). Interpolation reduces the large period step of approximately 1.2 [mm] of copper markings to a resolution smaller than 1 micrometer [55].

The encoder is designed in such a way, such that the encoder is robust to external electromagnetic interference [55]. The receiving coils are paired and of different polarity, and whenever interference comes in the system, the induced potential is in the coil pair adds up to zero. Furthermore, the encoder is robust to dust and other contaminations, and has a large temperature range.

2.7 Conclusion: Motor & Encoder Choice

This chapter has provided information regarding the workings of a linear motor; the different type of linear motors; information regarding cogging and how to reduce the effect of cogging; the different methods of commutation and different encoders that can be used to design one's own linear motor.

Since the goal of this thesis is to design a low-cost linear (direct-drive) motor specifically for low-duty CNC machines, one has to choose a fitting type of linear motor and encoder that is of low complexity, and is able to achieve the required performance. A comparison between the different linear motors is performed and presented in the morphological overview, see Appendix 6.4. The motors are distinguished on the output thrust; the amount of cogging present; weight; manufacturing cost (including assembly complexity) and efficiency based on the information given in this chapter. These factors have the same weight factor and are rated from $1 - 5$, the higher the better. In the end, the total gives the best motor choice.

It's been found that the iron-less tubular linear motor is a very prosperous candidate, because of its high actuator stiffness; no cogging; low weight; easy manufacturability and high efficiency (power density). The motor is easy to manufacture, since coils are directly wound on a coil holder and the magnets are easily clamped in the stator's tube. The stator also acts as the linear guide of the linear axis, reducing the total complexity of the drive system, which results in an optimal well integrated design that is low-cost. Furthermore, the actuator has great heat dissipation; a non-critical airgap; a very wide speed range and is very smooth in motion. For these reasons, this actuator has been selected for further development. SVPWM and Field Oriented Control will be implemented to improve on actuation smoothness and total efficiency.

The encoder choice mainly depends on the total cost of the encoder and the application. Since low-duty CNC machines generally work at room temperature and include an enclosure, such that dust and other contaminations are significantly reduced, a low-cost incremental optical encoder has been selected. Furthermore, since the encoder is immune to electromagnetic interference and solely relies on (infra-red) light, the encoder does not have to be shielded, reducing the total complexity.

Optical encoders dominate the industry and are widely used. The encoder that is selected is shown in Appendix C1 and is used in large-scale paper printers, which can achieve a minimum resolution of 17.8 micrometer at a maximum pulse frequency of 80 kHz, which relates to a maximum speed of 5.6 m/s. Furthermore the cost per complete set-up is under €10,-/meter.

Chapter 3

Design & Optimization Of The Tubular Linear Motor

3.1 Introduction

In this chapter, the design and optimization of the tubular linear motor will be discussed. First the requirements and the objective of the optimization is presented. An analytical model of the tubular linear motor is given. And in order to get a better understanding on the motor's behavior, both a generator and a motor COMSOL model are presented. The COMSOL motor model is then used for (brute force) optimization, which is performed in MATLAB. The control and its algorithms are then explained in the follow-up section, which is designed in the MATLAB SIMULINK environment. The chapter closes with a concluding CAD motor design. This chapter's process is shown in figure 3.1.

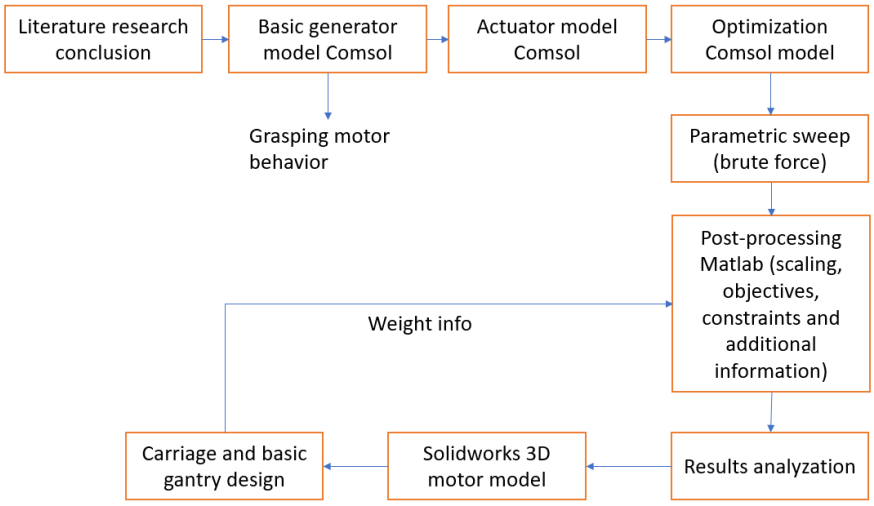

Figure 3.1: Design methodology of this chapter.

3.2 Optimization & Requirements

Multiobjective optimization:

- Minimize: *Total cost* → Cost reduction and weight saving (x2)
- Minimize: *Power usage* → heat reduction rotor, and efficiency (x1)

Given constraints:

- $h_1(x)$: Acceleration = 11 [m/s^2] (+10% for unaccounted effects)
- $h_2(x)$: Estimation extra weight ex. rotor
  - E3D volcano: ~0.2 [kg]
  - Carriage: ~0.2 [kg]
- $h_3(x)$: Friction constant: 0.4 (worst case IGUS Iglidur® bearing)
- $h_4(x)$: Wiresizes: 0.45...0.05...0.6 [mm]
- $h_5(x)$: Rotor length: 65 [mm]
- $h_6(x)$: Axis length: 500 [mm]
- $h_7(x)$: Coil (rotor) length: 10 [mm]
- $h_8(x)$: Spacer (rotor) length: 0.8 [mm]
- $h_9(x)$: Air gap: 3 [mm]
- $h_{10}(x)$: Densities of Brass, Copper, 3D print material and NdFeB (CES Edupack).
- $h_{11}(x)$: Price of Brass, Copper, 3D print material and NdFeB (CES Edupack/China import).
- g(x): Max DC current < 3 [A]
- g(x): Max Power < 20 [W]

Figure 3.2: Optimization objectives and requirements: h(x): fixed constraint; g(x): inequality constraint.

The goal of this thesis is "the design and manufacturing of a low-cost direct-drive motor, that is specifically optimized for low-duty CNC machines in performance and cost". The tubular linear motor is selected, that uses a low-cost optical encoder. The first objective is to minimize the total cost of the rotor and stator combined, which is directly related to a reduction in weight. A low weight is preferred, since the motor in its entirety may be incorporated in a gantry design that uses two y-axes and one x-axis.

The other objective is to minimize the total power usage and increase efficiency. A motor can be very cheap, however a different motor design may be more efficient, which reduces the amount of heat dissipation required. This directly reduces the total cost of the motor, since less advanced cooling is required.

The minimum acceleration for positioning is to be 10 $[\frac{m}{s^2}]$. 10% has been added in order to account for unexpected effects.

The carriage's estimated weight excluding the rotor is expected to be about 0.4 [kg]. This includes the material of which the carriage is made of; the cooling fans for an E3D Volcano 3D printer head; the cooling fan intended for the motor; the encoder and wiring.

Since the design is to be as simple as possible and easily assembled, flanged sliding bearings are used. These are quiet and have a long life-time for this given load. The friction coefficient is generally around 0.15, however increases to 0.4 in the worst case scenario. A data sheet of this

bearing is shown in Appendix C2.

Different wire sizes give different results. For square magnet wire, excluding the insulator of the wire, the current density of the coil does not change for different wire sizes (current density is introduced in section 3.3). For round wire, there are however gaps in-between the wires, which reduces the total current density of the electromagnetic coil. For that reason smaller wire sizes are preferred. However, smaller wire also has less conductive material in its cross-section, since the area occupied by the insulation relative to the area occupied by the conductive material is larger. I.e. the fill factor is worse for smaller wire, which also reduces the current density of the electromagnetic coil. For this reason, a range of wire sizes has been selected (0.45 to 0.6 $[mm]$), such that we can study how this influences motor parameters.

Several motor constraints are given, such as the stator (axis) length; the rotor length; spacer length and the air gap. These are taken such that the design is 3D printable. Smaller spacers for example would allow for more windings, however loses its stiffness. Furthermore the material densities and costs are included, which are extracted from CES Edupack (and Chinese stores).

Furthermore, a current limiter has been included. This is to minimize heat in the PCB traces, and to limit current for the triple H-bridge (data sheet in Appendix C3). The triple H-bridge can handle up to 5 $[A]$ DC, however a margin of 2 $[A]$ has been included for safety and long life time. These currents are the equivalent DC currents of an AC signal. For a sinusoid $current_{DC} = \frac{1}{sqrt(2)} peakcurrent_{AC}$.

Finally a maximum power of the motor is defined to be 20 $[W]$. The amount of heat is similar to that of a portable loudspeaker and should thus not require special cooling, e.g. water cooling.

3.3 Analytical Model Of A Tubular Linear Motor

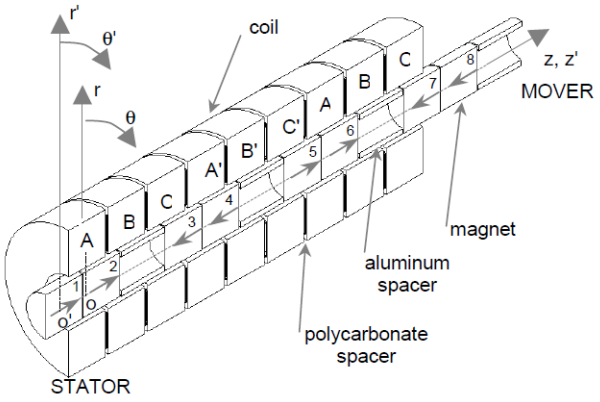

Figure 3.3: Schematic motor model (cylindrical coordinate system) that corresponds to the analytical model [43].

The following in-depth analytical model is given. A basis for this model comes from source: [43], however lacked in-depth explanation; is incomplete and does not explain under what conditions

this model is valid. The corresponding schematic model is shown in figure 3.3. The motor represents an iron-less tubular linear motor with an under-hung configuration. An under-hung design means that the individual coils are smaller than the permanent magnets. The opposite is named an over-hung design. An over-hung coil uses the magnetic flux more effectively, while the position dependency is more evenly smoothed' out. However, a large amount of windings are not effectively being used with as result an increase in weight of the moving mass [54]. It's a typical choice to choose for an under-hung design when the cost of the permanent magnets outweighs the efficiency, which is the case in this thesis report. For that reason, an under-hung design is opted for. In this particular design two coils are used for a single phase, but are of different polarity. These coils are to compensate for the current density that would otherwise have been greater in the case of an over-hung design.

3.3.1 Lorentz Force

The force between one magnet and one coil can be determined using the Lorentz force equation:

$$\boldsymbol{f} = \int (\boldsymbol{J} \times \boldsymbol{B})\, dV \tag{3.1}$$

Due to symmetry of cylindrical coordinate system, the electric current density will reduce to:

$$\boldsymbol{J} = J_\phi(r)\, \boldsymbol{i_\phi} \tag{3.2}$$

Substituting gives:

$$\boldsymbol{f} = \int (J_\phi\, \boldsymbol{i_\phi}) \times (B_r\, \boldsymbol{i_r} + B_\phi\, \boldsymbol{i_\phi} + B_z\, \boldsymbol{i_z})\, dV \tag{3.3}$$

$$\boldsymbol{f} = \int (-J_\phi \times B_r)\, \boldsymbol{i_z} + (J_\phi \times B_z)\, \boldsymbol{i_r}\, dV \tag{3.4}$$

Which again can be reduced, since the forces in the radial direction will cancel one another.

$$F_z(z) = \int (-J_\phi \times B_r)\, dV = \int (-J_\phi \times \mu_0 H_r)\, dV \tag{3.5}$$

We thus require H_r, the radial component of $\boldsymbol{H}$. The next section will help us find the final expression by using the scalar magnetic potential.

3.3.2 Scalar Magnetic Potential

For a magnetic field it goes that:

$$\boldsymbol{B} = \mu_0(\boldsymbol{H} + \boldsymbol{M}) \tag{3.6}$$

Where $\boldsymbol{B}$ has the SI units [$\boldsymbol{T} = \frac{V \cdot s}{m^2}$], μ_0 is in [$\frac{V \cdot s}{A \cdot m}$], and both $\boldsymbol{H}$ and $\boldsymbol{M}$ are in [$\frac{A}{m}$]. Here $\boldsymbol{H}$ represent the magnetic field intensity away from the source, and $\boldsymbol{M}$ the magnetization of the

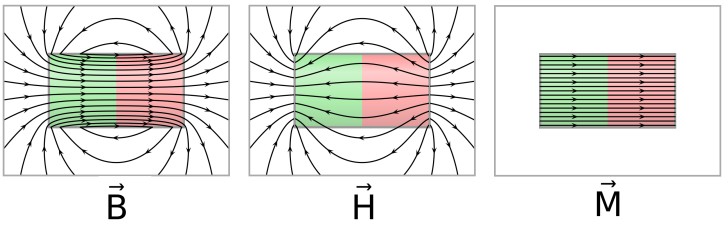

Figure 3.4: Differences B, H, M. Here B represents the magnetic flux density [T], H represents the magnetic field (intensity) lines outside the magnet [A/m], and M represents the magnetization field [A/m].

source. Furthermore, according to Gauss's law, the magnetic field's divergence equals zero, since the magnetic flux that exits the enclosed volume equals the magnetic flux entering the volume. With other words, the flux lines form a closed loop. Gauss's law thus says:

$$\boldsymbol{\nabla} \cdot \boldsymbol{B} = \mu_0(\boldsymbol{\nabla} \cdot \boldsymbol{H} + \boldsymbol{\nabla} \cdot \boldsymbol{M}) = 0 \tag{3.7}$$

Solving this equation gives us:

$$\boldsymbol{\nabla} \cdot \boldsymbol{H} = -\boldsymbol{\nabla} \cdot \boldsymbol{M} \tag{3.8}$$

Since the magnetic field intensity decreases over distance and is thus dependent on the position within that field, one requires a relation between the magnetic field intensity and position within that field. For an irrotational (conservative) vector field $\boldsymbol{E}$, one may determine the scalar potential ψ for a 3-dimensional Euclidean space as:

$$\psi = \frac{1}{4\pi} \int_{\mathbb{R}^3} \frac{\boldsymbol{\nabla} \cdot \boldsymbol{E}(\boldsymbol{r'})}{|\boldsymbol{r} - \boldsymbol{r'}|} dV(\boldsymbol{r'}) \tag{3.9}$$

So that $\boldsymbol{E} = -\boldsymbol{\nabla}\psi$. Here $\boldsymbol{r}$ defines the positional vector in the Euclidean space which we're interested in, and $\boldsymbol{r'}$ defines the positional vector of the magnet. In order to define the scalar potential, the following has to be true for vector field $\boldsymbol{E}$ to be irrotational (conservative):

1. $-\int_{\boldsymbol{a}}^{\boldsymbol{b}} \boldsymbol{E} d\boldsymbol{l} = \psi(\boldsymbol{b}) - \psi(\boldsymbol{a})$
2. $\oint \boldsymbol{E} d\boldsymbol{l} = 0$
3. $\boldsymbol{\nabla} \times \boldsymbol{E} = 0$

The first item implies that the line integrals through a gradient field are path independent according to the 'Fundamental theorem of calculus for line integrals', or also known as the 'Gradient theorem'. In physics this goes for a conservative force. The line integral of the gradient (conservative) field ($-\boldsymbol{\nabla}\psi$) thus only depends on its scalar potential at the initial and final positions.

The second integral implies that the line integral of the gradient field for a closed loop equals zero. Based on the previous item, this means that the final position equals the initial position.

The third item is a re-expression of the second item in terms of curl.

The magnetic field intensity $\boldsymbol{H}$ fits these requirements when there are no free currents ($\boldsymbol{J}$ $[\frac{A}{m^2}]$) and no change in the electric field $\boldsymbol{E}$, e.g. for a permanent magnet. Because, according to Ampère's law this results in $\boldsymbol{\nabla} \times \boldsymbol{H} = 0$. Thus for the scalar magnetic potential one finds (using eq. 3.8 and eq. 3.9):

$$\psi = \frac{1}{4\pi} \int_{\mathbb{R}^3} \frac{\boldsymbol{\nabla} \cdot \boldsymbol{H}(\boldsymbol{r'})}{|\boldsymbol{r} - \boldsymbol{r'}|} dV(\boldsymbol{r'}) = -\frac{1}{4\pi} \int_{\mathbb{R}^3} \frac{\boldsymbol{\nabla} \cdot \boldsymbol{M}(\boldsymbol{r'})}{|\boldsymbol{r} - \boldsymbol{r'}|} dV(\boldsymbol{r'}) \tag{3.10}$$

And $\boldsymbol{H} = -\boldsymbol{\nabla}\psi$. It's opted to use M, since M acts as the source of the magnetic field, and thus the magnetic potential.

When the permanent magnet is uniformly magnetized, e.g. the magnetization $\boldsymbol{M}$ remains constant, the following approach proves to be useful (Classical Electromagnetic Theory - van der Linde [40]).

Intuitively we expect that the exposed ends of the magnetic dipoles to be like magnetic surface charges (poles). At these ends, $\boldsymbol{M}$ is discontinuous and thus its divergence is singular, and the above integral cannot be evaluated. To deal with this discontinuity, we divide the body τ of the magnet in two separate regions τ_1 and τ_2. Here τ_1 ends at distance ε and τ_2 begins at distance ε and extends past the outer edge of the original volume of integration τ:

$$\psi = -\frac{1}{4\pi} \int_{\tau_1} \frac{\boldsymbol{\nabla} \cdot \boldsymbol{M}(\boldsymbol{r'})}{|\boldsymbol{r} - \boldsymbol{r'}|} dV(\boldsymbol{r'}) - \frac{1}{4\pi} \int_{\tau_2} \frac{\boldsymbol{\nabla} \cdot \boldsymbol{M}(\boldsymbol{r'})}{|\boldsymbol{r} - \boldsymbol{r'}|} dV(\boldsymbol{r'}) \tag{3.11}$$

Using the product rule $\boldsymbol{\nabla} \cdot (f\boldsymbol{M}) = \boldsymbol{\nabla} f \cdot \boldsymbol{M} + f\boldsymbol{\nabla} \cdot \boldsymbol{M}$ we recast the second term of the previous equation.

$$\frac{1}{4\pi} \int_{\tau_2} \frac{\boldsymbol{\nabla} \cdot \boldsymbol{M}(\boldsymbol{r'})}{|\boldsymbol{r} - \boldsymbol{r'}|} dV(\boldsymbol{r'}) = \frac{1}{4\pi} \int_{\tau_2} \boldsymbol{\nabla} \cdot \left(\frac{\boldsymbol{M}(\boldsymbol{r'})}{|\boldsymbol{r} - \boldsymbol{r'}|}\right) dV(\boldsymbol{r'}) - \frac{1}{4\pi} \int_{\tau_2} \frac{\boldsymbol{M}(\boldsymbol{r'})(\boldsymbol{r} - \boldsymbol{r'})}{|\boldsymbol{r} - \boldsymbol{r'}|}) dV(\boldsymbol{r'}) \tag{3.12}$$

Due to the divergence theorem as surface integrals, one for the inner ($\boldsymbol{S'}$) and one for the outer surface ($\boldsymbol{S''}$):

$$\begin{aligned} \frac{1}{4\pi} \int_{\tau_2} \frac{\boldsymbol{\nabla} \cdot \boldsymbol{M}(\boldsymbol{r'})}{|\boldsymbol{r} - \boldsymbol{r'}|} dV(\boldsymbol{r'}) =& \frac{1}{4\pi} \oint_{\boldsymbol{S'}} \frac{\boldsymbol{M}(\boldsymbol{r'})}{|\boldsymbol{r} - \boldsymbol{r'}|} d\boldsymbol{S'}(\boldsymbol{r'}) ... \\ &+ \frac{1}{4\pi} \oint_{\boldsymbol{S''}} \frac{\boldsymbol{M}(\boldsymbol{r'})}{|\boldsymbol{r} - \boldsymbol{r'}|} d\boldsymbol{S''}(\boldsymbol{r'}) - \frac{1}{4\pi} \int_{\tau_2} \frac{\boldsymbol{M}(\boldsymbol{r'})(\boldsymbol{r} - \boldsymbol{r'})}{|\boldsymbol{r} - \boldsymbol{r'}|}) dV(\boldsymbol{r'}) \end{aligned}$$

The second integral vanishes, since $\boldsymbol{M}$ is zero at the exterior boundary. The third integral also vanishes when we let ε tend to zero, while $\boldsymbol{S'}$ will tend to the boundary $\boldsymbol{S}$ of the magnetized material. We note however, that $\boldsymbol{S'}$ is the outward-pointing surface of $\boldsymbol{S}$. Thus $\boldsymbol{S} = -\boldsymbol{S'}$. Substituting gives the final expression for the scalar magnetic potential:

$$\psi = -\frac{1}{4\pi}\int_{\tau_1}\frac{\boldsymbol{\nabla}\cdot\boldsymbol{M}(\boldsymbol{r'})}{|\boldsymbol{r}-\boldsymbol{r'}|}dV(\boldsymbol{r'}) + \frac{1}{4\pi}\oint_{\boldsymbol{S}}\frac{\boldsymbol{M}(\boldsymbol{r'})}{|\boldsymbol{r}-\boldsymbol{r'}|}d\boldsymbol{S}(\boldsymbol{r'}) \tag{3.13}$$

For a cylindrical magnet that is uniformly magnetized over its length L, the first term disappears, since the divergence is zero. Only the surface integrals remain, and for convenience, we place the origin in the center of the magnet:

$$\psi = \frac{1}{4\pi}\oint_{rightface}\frac{\boldsymbol{M}(\boldsymbol{r'})}{|\boldsymbol{r}-\boldsymbol{r'}|}d\boldsymbol{S}(\boldsymbol{r'}) - \frac{1}{4\pi}\oint_{leftface}\frac{\boldsymbol{M}(\boldsymbol{r'})}{|\boldsymbol{r}-\boldsymbol{r'}|}d\boldsymbol{S}(\boldsymbol{r'}) \tag{3.14}$$

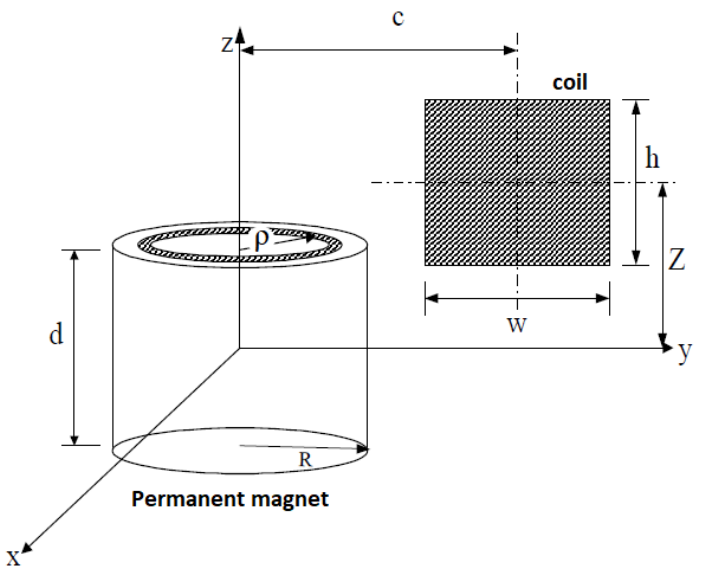

Figure 3.5: Permanent magnet positioned in the center, having the coil revole around the permanent magnet. The variables in the picture are associated to the analytical model. Source: Design of a Novel-Direct TLBPMM - Kim. W

Using equation 3.14 and figure 3.5 results in the following expression:

$$\begin{aligned}\psi =& \frac{M}{4\pi}\left[\int_0^R\int_0^{2\pi}\frac{\rho}{\sqrt{(z-\frac{d}{2})^2+r^2+\rho^2-2r\rho\cos(\theta-\phi)}}d\theta d\rho... \right.\\ &\left. -\int_0^R\int_0^{2\pi}\frac{\rho}{\sqrt{(z+\frac{d}{2})^2+r^2+\rho^2-2r\rho\cos(\theta-\phi)}}d\theta d\rho\right]\end{aligned}$$

Then we find the magnetic field as:

$$\boldsymbol{H} = -\boldsymbol{\nabla}\cdot\psi = \frac{-M}{4\pi}\boldsymbol{\nabla}\cdot\left[\int_0^R\int_0^{2\pi}\frac{\rho}{\sqrt{(z-\frac{d}{2})^2+r^2+\rho^2-2r\rho\cos(\theta-\phi)}}d\theta d\rho... - \int_0^R\int_0^{2\pi}\frac{\rho}{\sqrt{(z+\frac{d}{2})^2+r^2+\rho^2-2r\rho\cos(\theta-\phi)}}d\theta d\rho\right]$$

And in the radial direction:

$$H_r = -\frac{d\psi}{dr} = \frac{-M}{4\pi}\frac{d}{dr}\left[\int_0^R\int_0^{2\pi}\frac{\rho}{\sqrt{(z-\frac{d}{2})^2+r^2+\rho^2-2r\rho\cos(\theta-\phi)}}d\theta d\rho... - \int_0^R\int_0^{2\pi}\frac{\rho}{\sqrt{(z+\frac{d}{2})^2+r^2+\rho^2-2r\rho\cos(\theta-\phi)}}d\theta d\rho\right]$$

Substituting this expression in the Lorentz force equation 3.5, we find:

$$F_z(Z) = \frac{J\mu_0 M}{4\pi}\int_{ID/2}^{OD/2}\int_{Z-h/2}^{Z+h/2}\int_0^{2\pi}\frac{d}{dr}\left[\int_0^R\int_0^{2\pi}\frac{\rho}{\sqrt{(z-\frac{d}{2})^2+r^2+\rho^2-2r\rho\cos(\theta-\phi)}}d\theta d\rho... \tag{3.15}$$

$$- \int_0^R\int_0^{2\pi}\frac{\rho}{\sqrt{(z+\frac{d}{2})^2+r^2+\rho^2-2r\rho\cos(\theta-\phi)}}d\theta d\rho\right] r\,d\phi\,dz\,dr \tag{3.16}$$

This analytical model thus gives us the Lorentz force of a coil with current density J and a magnet with magnetization M for an iron-less tubular linear motor given permanent magnet and coil parameters. OD and ID are the outer and inner diameters of the coil and the other values are shown in figure 3.5.

The model is rather complex and only outputs the Lorentz force. In order to get a better grasp on the motor's behavior and to simplify the optimization process, a COMSOL motor model is designed, which is discussed in the next section.

3.4 COMSOL Finite Elements Model

As explained in the previous section, an under-hung design is opted for. In order to get a better grasp on the motor concept, both a generator and motor COMSOL model are made. The goal is to extract important information, such as the motor constant, electrical information and motor behavior. This information is then used for the optimization.

3.4.1 Geometric Design & General Definitions

Below shows the base geometry and neutral position of the COMSOL generator/motor model used. The design is an axisymmetric design that includes the permanent magnets (grey); the

permanent magnet spacers (dark green); a brass tube (orange); air (light blue); the electromagnetic coils (yellow) and the coil spacers (light green). The black arrows indicate the permanent magnet directions and the red arrow indicates the direction of travel for both the generator and motor model. The thick red line shows the axisymmetric line around which the motor is revolved.

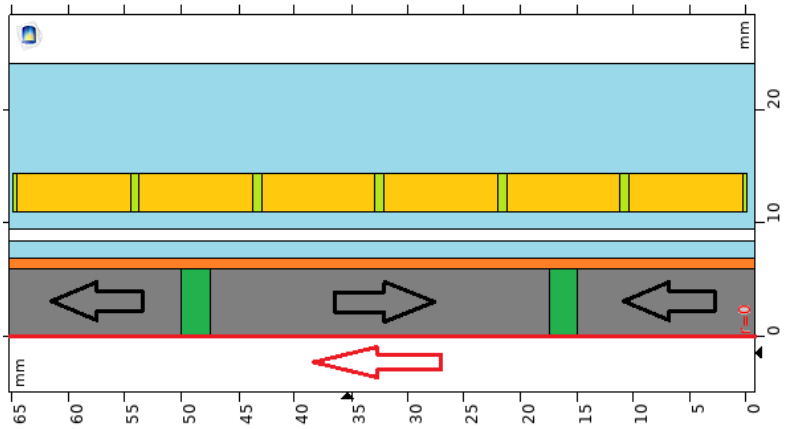

Figure 3.6: Tubular linear motor model in COMSOL. Axisymmetric design (red line).

.

A brass tube has been opted for, since the material is non-magnetic. Furthermore, the electrical conductivity of brass is significantly lower than for example aluminium and copper (28 %, to 61 % and 100 %) [58]. This results in reduced eddy current damping due to Lenz law, which is induced by the changing magnetic field of the electromagnetic coils. The spacers of both the rotor and stator are made of non-ferromagnetic material, and are 3D printed with special heat resistant plastic.

The permanent magnets are ordered from China and have N50 magnetization, which equals to 1.4-1.45 [T] [20]. In this COMSOL model, 1.4 [T] has been used for the magnetic remanence of the permanent magnets.

The current dimensions used in the above drawing are the optimized dimensions for convenience. For both the generator and the motor model these dimensions are used for consistency. The models use a parameter list (in COMSOL) which can be found in Appendix C4. Appendix C4 also lists model set-up in more detail. These parameters define the fixed dimensions; calculate the required spacer dimensions; define the rotor speed of the generator model; define the required peak current for the motor model and define the magnetic remanence of the permanent magnets.

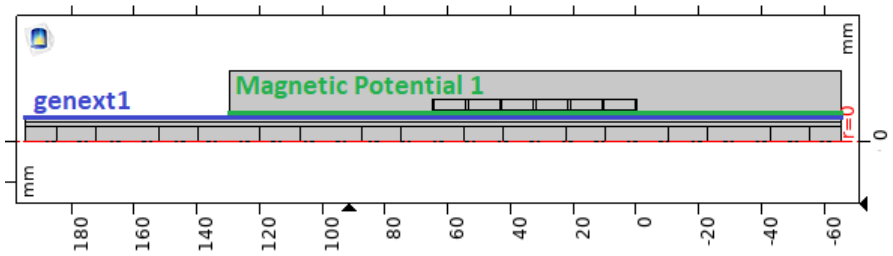

Figure 3.7: A general extrusion is defined and used in the 'Magnetic Potential 1' to couple the two air boundaries.

The model consists of a static part (the stator) and a moving part (the rotor). In order to model these, 2 selections are made under definitions of the component (see Appendix C4). The rotor and the stator have an undefined gap in-between. In order to correct for this gap and have the two boundaries of the air pockets act as one, a general extrusion is defined for the bottom boundary (see figure 3.7). This general extrusion is then used in the 'Magnetic Potential 1' of the 'Magnetic Field' physics, which couples the two boundaries together (see Appendix C4). Furthermore a 'Perfect Magnetic Conductor 1' has been added to the upper boundary, such that there are no losses between the two boundaries.

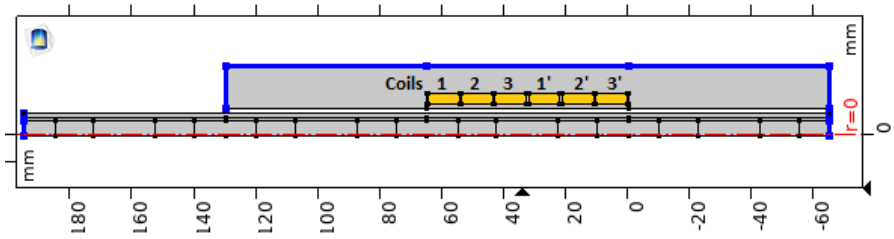

Figure 3.8: Coil numbers (names) and magnetic insulation.

.

Figure 3.8 lists the coil numbers, which are used as coil names in the COMSOL models. These coils are defined under the 'Magnetic Fields' physics. Here the amount of windings; the cross-section of the wire and DC current are defined. The same figure also lists the magnetic insulation. These are defined, such that the compiler knows there is no magnetic interaction beyong these boundaries. These boundaries are positioned such that the magnetic field lines of the permanent magnets are well established before interacting with the electromagnetic coils (see figure 3.9).

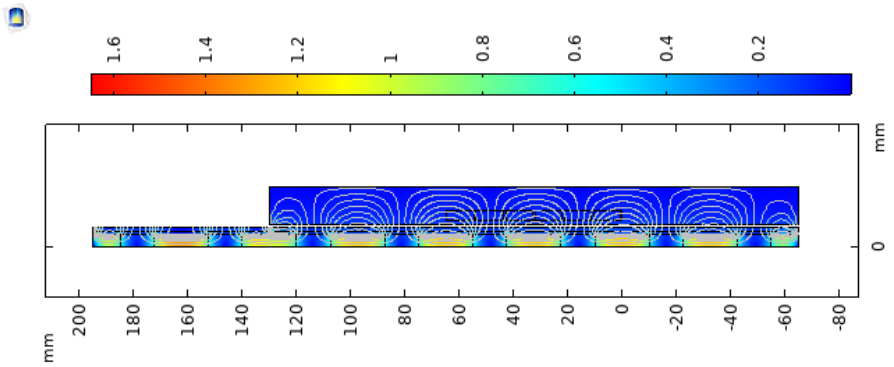

Figure 3.9: The magnetic field lines are well established with an air pocket of this size (rotor).

.

More detailed information regarding the model set-up can be found in Appendix C4.

3.4.2 Generator Model

In order to make the rotor move compared to the stator, a time-dependent study is selected. The generator model requires an extra definition in order to create motion. The variable list in Appendix C4 defines the rotor speed as 1000 $[\frac{mm}{s}]$. Since the rotor and stator pitch are 65 $[mm]$, the rotor moves at a frequency of about 15.4 Hz. This frequency is used as the slope of a ramp function, which is then used in a 'Moving Mesh'. The moving mesh moves to the left, with a position defined as: $pitch_{rotor} * rm1(t[1/s])$, where $rm1$ is the ramp function that is a function of time (see Appendix C4: Generator Model). Now when the study runs, the rotor will be properly positioned for each time step and 'move' at constant speed.

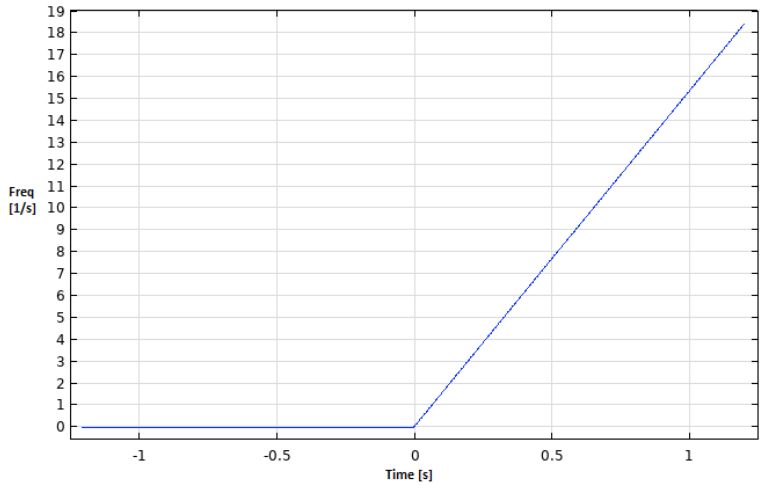

Figure 3.10: Ramp definition with the frequency as slope is used for motion creation within COMSOL.

The reason why the motor is moved with a speed of 1000 $[\frac{mm}{s}]$ is to find the motor constant from the induced voltages. We know from Faraday's law that for a Lorentz actuator (with windings orthogonal to magnetic field), the induced voltage is:

$$V_m = n\frac{d\phi_w}{dt} = n\frac{d\phi_w}{dx}\frac{dx}{dt} \tag{3.17}$$

$$Bl_w = \frac{dx}{dt} \tag{3.18}$$

$$V_m = Bl_w n\frac{dx}{dt} = k\frac{dx}{dt} \tag{3.19}$$

Here V_m is the induced back electromotive force in the motor; ϕ_w is the magnetic flux in the windings; l_w the effective winding length in the magnetic field; n the amount of windings; $\frac{dx}{dt}$ the speed at which the rotor moves and k the motor constant.

If the rotor moves at a constant speed of 1 $[\frac{m}{s}]$ (or 1000 $[\frac{mm}{s}]$), the motor constant can directly be extracted by combining the absolute induced voltages of the electromagnetic coils. The result is shown in figure 3.11.

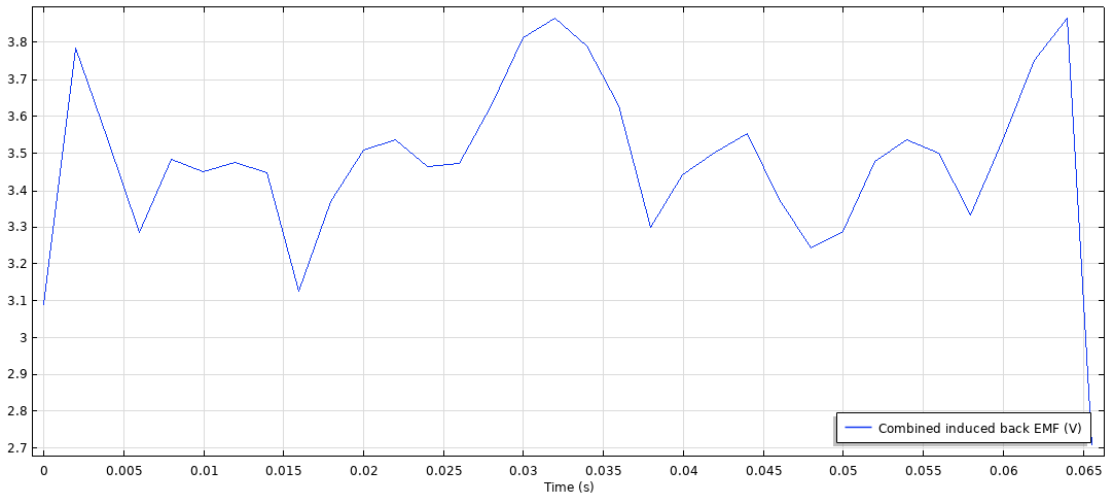

Figure 3.11: By combining the induced EMF of each coil, the motor constant can be extracted.

The average is approximately 3.5 $[V]$, which equals to the motor constant in $[\frac{N}{A}]$ according to the theory. This value will be compared and validated with the motor constant found in the COMSOL motor model.

The motor appears to have 6 phases that are 60 electrical degrees apart as can be seen in figure 3.12. However, by having a closer inspection, it can be noted that it's actually a three phase system. Two coils of each pair are of different polarity, and by combining these, a three phase signal is achieved (see figure 3.13). This tells us how the motor should be wired in order

to commutate properly. Furthermore, it can be seen that each cycle takes 0.065 seconds. At a speed of 1 $\frac{m}{s}$ this validates the magnetic pitch to be 65 [mm].

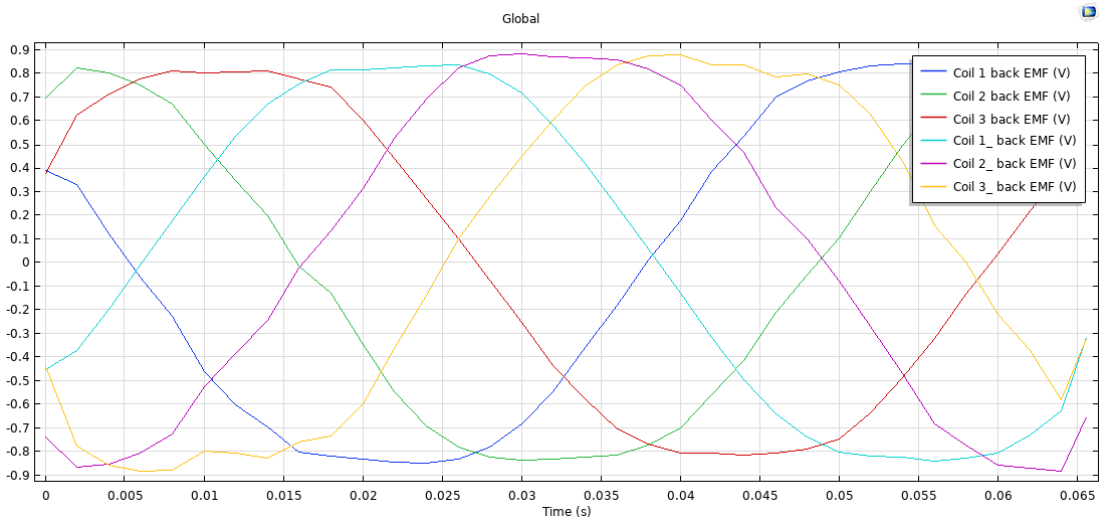

Figure 3.12: Induced EMF of each electromagnetic coil. The coil names relate to 3.8.

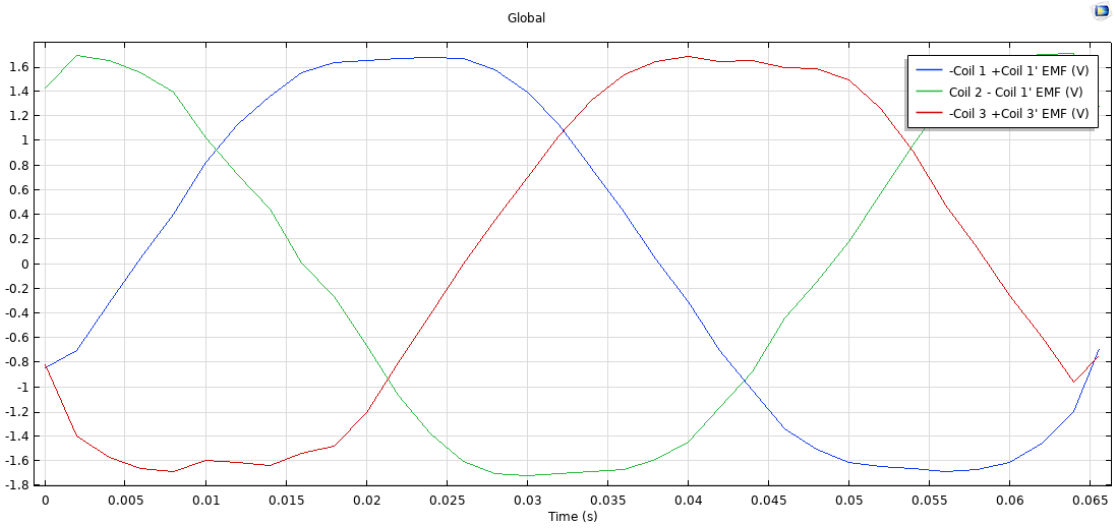

Figure 3.13: Induced EMF of each phase, which is a combination of each coil pair. The coil names relate to 3.8.

This model runs in about 1 minute and 10 seconds, which is non-ideal for a brute force optimization where hundreds of motor models are simulated that are of different parameters. Furthermore, the motor constant is not easy to extract. For these reasons, a motor model that extracts the instantaneous Lorentz force is made and shown in the next section.

3.4.3 Motor Model

Since the Lorentz force is instantaneous, a time-dependent study is not required. A stationary study suffices, which greatly improves the computation time.

In order to extract the motor constant, we again require new definitions. Three wave forms (wv1; wv2; wv3) are defined that are sinusoidal in shape (see figure 3.14). These represent the 3-phase current. They have an angular frequency of $\frac{2\pi}{rotor_{pitch}}$ and are separated by 120 electrical degrees. The amplitude of each sinusoid is defined as $sqrt(2)$ $[A]$, which means that the equivalent DC current of each coil is 1 $[A]$. The wave forms are thus a function of the position along the stator from the neutral position. The equivalent DC current is used, since a basic Lorentz actuator generally uses plain DC current. In order to find similar results with the generator model where Faraday's law is used for a Lorentz actuator, consistency is key. Furthermore, the equivalent DC current is used for the power calculation of each motor model.

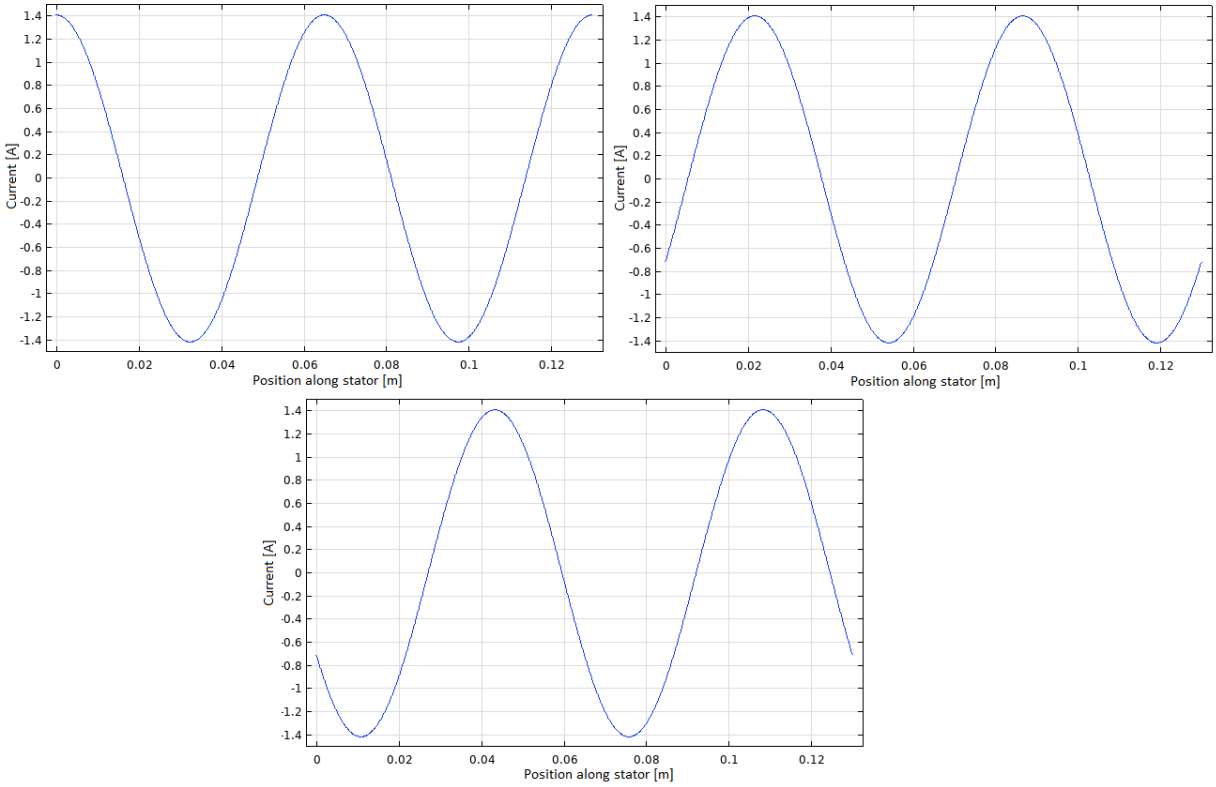

Figure 3.14: From left to right: definition wv1; wv2 and wv3, which are the 3 phase current wave forms that are a function of the position along the stator. The peak of each current wave form is $sqrt(2)$ $[A]$, whose equivalent DC current is 1 $[A]$.

Since the study is stationary, only the currents for the neutral position are extracted (wv1(0); wv2(0) and wv3(0)). These are then properly matched with the correct electromagnetic coils in 'Coil 1', 'Coil 2', 'Coil 3' of the 'Magnetic Fields' physics, and similarly for their respective counterparts (see Appendix C4: Motor model) based on the wave form information extracted from the Generator model.

After running the simulation, a surface integration within COMSOL (2D-axisymmetric study) calculates the Lorentz force of all electromagnetic coils combined. The value found is 3.72 [N], which is very similar to the 3.5 $[V]$ found in the generator model.

The total computation time required for a single study is merely 5 seconds, which is a great improvement over the generator model. This model is extended to a parametric design study used for the optimization, which is explained in the next sub section.

3.4.4 Parametric Sweep For Optimization

The method of optimization used in this report is brute force optimization. A variety of motor models are considered for each wire size. In the parametric sweep, we change the variables listed in figure 3.15. The conductive wire diameters used are [0.45; 0.05; 0.6] and an insulation layer of 25 [µm] is added to the wire radius.

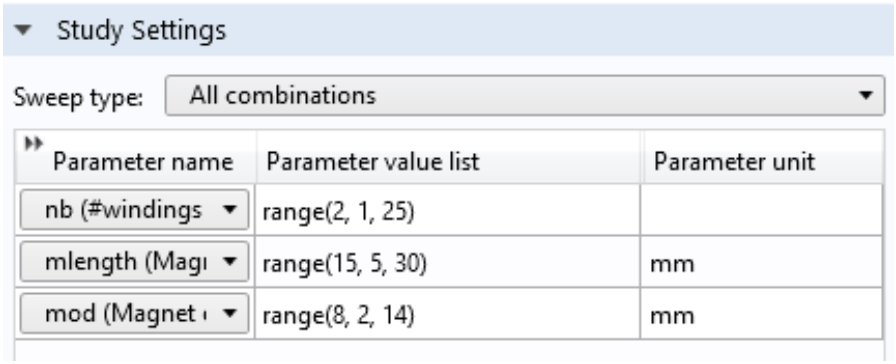

Figure 3.15: Parametric sweep for different motor models used for optimization.

'nb' stands for the number of windings in the radial direction and defines the coil thickness together with the wire diameter. The number of windings in the axial direction 'na' is fixed and calculated using the motor pitch (65 [mm]); the rotor spacers (0.8 [mm]) and the model's wire diameter. 'mlength' defines the permanent magnet length, which directly affects the magnetic flux density and the spacer lengths. 'mod' represents the magnet diameter, changing this value also changes the magnetic flux density. How other variables are affected can be seen in the parametric list in Appendix C4.

The total number of motor models calculated per wire size is thus $24 * 4 * 4 = 384$. Since four different wire sizes are used, the total number of motor simulations is thus 1536. One of these combinations would result in the ideal motor size.

From these optimization models the resistances and motor constants are exported and used in the Matlab post-processing. 'nobironforce.txt' gives a table with columns: [nb mlength mod motorconstant] and 'nobironresistance.txt' gives a table with columns [nb mlength mod coilresistance].

3.5 MATLAB Post-processing Optimization

In this section brute force optimization is used. The code is given in Appendix C5: Optimization code, and is explained here.

First the tables of all wire sizes are numbered from 1 to 4 (0.65 to 0.5 wire outer diameter) and are then combined in table 'combtable'. The columns of this table are:

[wire number (related to wire diameter); back iron; nb; magnet length; magnet diameter; motor constant; coil resistance]

Back iron has been included in this optimization for future use, however since an iron-less tubular linear motor is designed, this value is set to zero for all motor models. In the next section of the code, the standard dimensions; material information and the constraints are provided. The code then loops through 'combtable', and does the necessary calculations to check whether the particular motor model fits the constraints given in figure 3.2. If it fits the constraints, the particular motor model is added to the table 'opttable'. The columns of this table are:

[Required DC current; mass of stator; combined stator and rotor mass; required force; motor constant; price of stator; price of rotor; price combined; power usage; objective function]

The objective function is calculated in the next section of the code. Here different tables are first defined that extract the minima and maxima of the columns from 'opttable', e.g. 'powermin' provides the minimum power of all motor models. Similarly 'pricetotmin' gives the minimum total price for the cheapest motor.

The code now loops through 'opttable' that includes all motor models that fit the constraints, and calculates the (multi) objective function. The objective function is normalized and defined as:

$$obj = w_{power} * \frac{powermin}{power} + w_{price} * \frac{pricetotmin}{pricetot} \tag{3.20}$$

Here w_{power} is the weight factor that is used for the power objective, which is set to 1; w_{price} is the weight factor that used for the cost objective, which is set to 2. The 'power' and 'pricetot' are the variables that list the motor power and total price of the particular motor model. The objective is saved again in 'opttable'.

Finally, 'opttable' is sorted based on the objective function value from high to low. The best scoring motor model is at the top, whereas the worst motor model is at the bottom of the list. Appendix C5: Optimization results, shows the top 20 motor models for all wire sizes; the optimized values per wire size and the top 5 motor models per wire size.

From these results, it can be seen that the total price decreases with wire size, however the power usage generally increases, which was expected (see section 3.2). We find from the top 20 table, that only the top three motor models require permanent magnets with 10 $[mm]$ magnet diameter and 20 $[mm]$ magnet length. After that, permanent magnets of 25 $[mm]$ are required.

Wire with a diameter of 0.5 $[mm]$ is available in the university's work space. A motor model with 'wired' that is either 3 or 4 is opted for, since the isolation thickness of the wire is unknown. 'wired' 4 has been selected, and an extra layer of windings has been added ('nb' = 7'). This totals the number of windings per coil to be 140, with an estimated resistance of about 1.1 ohm per coil and thus 2.2 ohm per phase. This value should be slightly smaller in case the outer wire diameter is actually 0.55 $[mm]$, which relates to 'wired' 3. The motor constant should be around 3.7 $[\frac{N}{A}]$. The required power is about 20 $[W]$ with an equivalent DC current of 1.7 $[A]$. The estimated material cost for 0.5 $[m]$ stroke, excluding electronics, is expected to be below 25 euros.

The motor model that is opted for is selected with a red box in Appendix C5: Optimization results. In the next section, the control scheme that is developed is presented in MATLAB SIMULINK.

3.6 MATLAB SIMULINK Control

The main goal of this Thesis report is to create a low-cost direct-drive motor. Low-cost hardware, namely an Arduino is used as the brain of the motor. Initially a MATLAB SIMULINK model is developed that can be uploaded to the Arduino, however afterwards Arduino code is written, which drastically improved motor performance due to increased sampling rates. This report however only discusses the SIMULINK model and in particular the closed-loop SIMULINK MODEL, since the Arduino code is very much a-like.

A constant force SIMULINK MODEL had also been developed, which is used to find the motor constant in the next chapter (Validation & experiments motor demonstrator). In the same chapter, black-box identification is performed, which simplified the power control of the motor such that the motor constant and the impedances of the coils were no longer used. However as mentioned before, these models and scripts are not discussed in detail. The model in this chapter is very similar and only requires small modifications in order to change its function, e.g. a constant accelerating rotor that is used for measuring the motor constant.

The closed-loop SIMULINK model is shown in Appendix C6: SIMULINK model. The Arduino code can be found in Appendix C6: Motor control code. 'Vdc' represents the supply voltage and 'Tz' is the PWM period. These variables are used in the SVPWM algorithm. The SVPWM algorithm presented in Appendices 6.1 and 6.2 is implemented, however is not discussed in detail.

The SIMULINK model can be divided in four parts: PID control loop; start-up sequence; power management (including SVPWM) and encoder.

The model does basically the following:

1. Disable encoder information ('start-up 3' block)

2. Turn on the motor using block 'start-up 1' and 'motoron'. This block outputs 1.5 $[A]$ peak current of the three phase signal, which then passes through a saturation block that limits the current (DC equivalent of 3 $[A]$). The peak current is then converted to a peak voltage, where 'vref/amps' define the relation between the two (extracted from the next chapter). This relation is linear, since the output PWM frequency remains constant. Furthermore, since the inductance of the coils is low, little phase lag is present and thus an additional current controller is not re-

quired for Field Oriented Control. The peak voltage is then fed to the SVPWM control algorithm.

3. While the motor is turned on, the rotor is aligned with the magnetic field by setting the position in the electrical cycle to -90 degrees, which is fed to the SVPWM algorithm. The motor turns off again (block 'start-up 2'); the position in the electrical cycle is reset to zero and the encoder information is turned on again. This method assures that the total current vector is 90 electrical degrees of the magnetic field vector and defines the zero point. Control is initiated with the 'initiate control' block.

4. The encoder block converts the 2 channel block signals of the quadrature encoder to a position. Furthermore, this position provides an angle, that defines the position in the electrical cycle using the motor pitch. This angle is then used to properly commutate (switch the currents) in the SVPWM algorithm. The position is also fed to the PID controller for closed-loop position control. The encoder code can be found Appendix C6: SIMULINK model.

5. The PID controller tracks the required position, and outputs a peak force that is then converted to a peak current of the three phase signal using the motor constant. This current is then again fed to the power scheme and SVPWM algorithm to output the PWM signals for the triple H-bridge. The PWM signals operate at 20 [KHz], making the motor inaudible.

The above model works at a sampling frequency of about 150 [Hz] max in Simulink. Only a stable bandwidth of about 40 [Hz] could be achieved. For that reason this model has been converted to an Arduino code, where the sampling frequency is increased to 500 [Hz] with 130 [Hz] control bandwidth (see section 4.4). Furthermore, in the arduino code, the SVPWM basic waveform is saved in a look-up table to reduce delays and boost control loop performance.

A detailed representation of this SIMULINK control scheme can be found in Appendix C6: SIMULINK model.

3.7 Conclusion & CAD design

This chapter explained the methodology which was presented in figure 3.1. First the optimization objectives and constraints were discussed. Design choices were explained, such as the use of slide bearings and 3D printing.

Then an analytical model of the iron-less tubular linear motor is given, however a generator model provides better understanding on the motor's behavior. One is able to find the motor constant using the generator model and is able to figure out which coils form together a single phase.

Then a motor model was presented, which is able to shorten the computation time significantly that allows the engineer to extend this model to a parametric sweep, that is used for the brute force optimization. The resistances and motor constants of each motor model is saved and post-processed in MATLAB to find an optimized motor model.

The optimized motor constant found from the motor model (3.75 $[\frac{N}{A}]$) was very similar to the motor constant found from the generator model (3.5 $[\frac{N}{A}]$). The required power is approximately 20 $[W]$ and requires an equivalent DC current of approximately 1.7 $[A]$. The resistance of a single coil is expected to be 1.1 $[\Omega]$ (single phase: 2.2 $[\Omega]$). The material cost per motor for 0.5 $[m]$ stroke, excluding electronics, is estimated to be below 25 euros. The encoder, as mentioned

in section 2.7, costs approximately 10 euros per set (encoder + strip).

A control scheme was presented that includes a start-up scheme; encoder position information; PID closed-loop control and power management that includes SVPWM commutation.

A CAD model of the motor is provided in Appendix C7: CAD Motor Model, which takes these optimized parameters into account. The optimized parameters are used in the previous sections to showcase the COMSOL generator and motor model. The rotor spacers are made slightly thinner (0.6 $[mm]$ instead of 0.8 $[mm]$), such that 20 windings can fit more easily in the axial direction of the motor (outer wire diameter: 0.5 $[mm]$).

The stator uses a brass pipe with an inner diameter of 11 $[mm]$. Compared to other materials, brass has a lower electrical conductivity compared to for example aluminium or copper, which reduces eddy current damping. In the COMSOL simulation an inner diameter of 10 $[mm]$ is used, however due to the magnet tolerances one is unable to fit these magnets in this pipe. The permanent magnets are instead taped to a slightly larger diameter, such that they can fit in the 11 $[mm]$ brass pipe. This change in brass pipe diameter should not influence the optimization results, since the material is non-ferromagnetic and eddy damping due to Lenz law is found to be minimal. 10 $[mm]$ diameter permanent magnets with a length of 20 $[mm]$ were found to be ideal for this application given the constraints. Spacers of 12.5 $[mm]$ thickness are put in-between the permanent magnets, and are then clamped in its entirety by two 3D printed caps, which are glued in place.

Chapter 4

Validation & Experiments Demonstrator

4.1 Introduction

In this chapter, experiments are performed in order to validate the COMSOL model and the optimization results. First the demonstrator is presented, after which the electrical characteristics of the coils and the relationship between the current and the potential are determined. Then using an analog force gauge, the motor constant is determined. A black box identification is performed, which results in a control scheme that will no longer require a motor constant nor a current/voltage relation increasing control loop performance. The PD values are tuned, and different step sizes are tested that use a trapezoidal motion profile to find the position accuracy of the motor.

4.2 Demonstrator model

Below the demonstrator model is presented. The stator is 0.5 [m] in length; has an outside diameter of 12 [mm] and is made of brass. In the stator, NdFeB 1.4 [T] permanent magnets of 10 [mm] in diameter and 20 [mm] in length are inserted. 3D printed spacers of 12.5 [mm] are put in-between. A second (aluminium) tube has been added in order to counter rotations of the carriage. This tube is of the same dimensions as the brass tube. The stator and aluminium tube are clamped in 3D printed holders, that are attached to a stiff plate.

A PCB has been developed for the motor and is presented in Appendix C9: PCB & Electrical schematic, The components include the required resistors and capacitors; the motor driver; the connectors and the Arduino used. The wiring shows how these components are assembled. The estimated cost of a single (assembled) PCB is 20 euros.

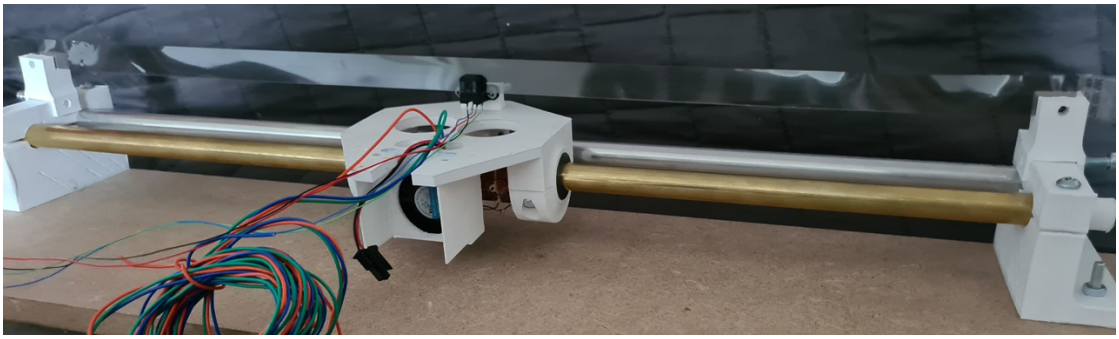

Figure 4.1: The demonstrator model used. The stator is the brass tube; an aluminium tube is used to counter carriage rotations and the carriage includes the rotor.

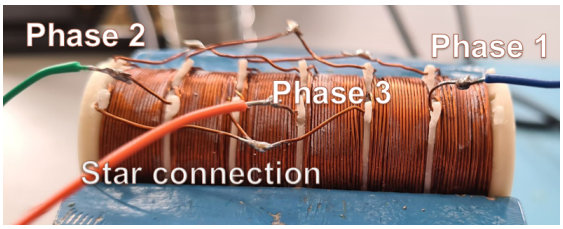

(a)

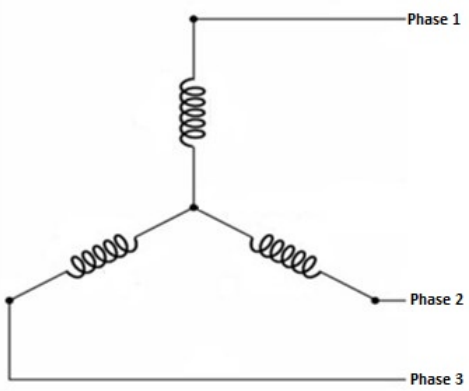

(b)

Figure 4.2:
(a) The iron-less tubular linear motor. The phases are connected in a star connection as shown in (b).

The carriage is 3D printed, and includes a small 30 [mm] axial fan, that cools the iron-less tubular linear motor. The carriage is very light-weight, since an infill percentage of 50 % is used, which results in a stiff yet light-weight design. The carriage does not include the 3D printer extrusion system, and is thus much lighter than what was required for the optimization. The total weight of the carriage, including the tubular linear motor; the slide bearings; the encoder and cooling is found to be 0.37 [kg]. The rotor alone weighs 0.29 [kg], which is very similar to what is found in the optimization model. As mentioned in the previous chapter, the total material cost is estimated to be below 25 euros.

A low-cost optical quadrature encoder is used, that uses an encoder strip with very fine lines at 71.1 [μm] apart. This allows for a minimum resolution of 17.8 [μ m].

The coils of each phase are connected, such that the second coil is of negative polarity compared to the first coil. The phases are then connected in a star connection as can be seen in figure 4.2b. The resistances and inductances of each phase are shown in table 4.1.

	Resistance [Ω]	Inductance [mF]
Phase 1 (green)	1.69	0.61
Phase 2 (blue)	1.74	0.62
Phase 3 (orange)	1.75	0.63

Table 4.1: Resistance and inductance of each phase.

These resistance values of each phase are smaller compared to what is found in the COMSOL model. This could be because the insulation layer is thicker than the 25 [µm] used in the COMSOL model, resulting in a smaller conductive cross-section. Furthermore, since the coils are hand-made, this explains the differences (< 5 % error) in values of each phase.

The inductance per phase is found to be very low and the effect is studied in a SIMULINK model. In this model, a sinusoidal potential that is made of 20 [KHz] PWM signals is fed to a single phase and the current is measured. Using the above electrical values, no phase lag is found and the magnitude appeared to follow ohm's law. This allows for a simple current/potential relation which is used in the SIMULINK control scheme presented in section 3.6 and Appendix C6: SIMULINK Model ('vref/amps'). The relation between the two is shown in figure 4.3 and is measured using current sensors that are connected to every phase. The resistance may be directly extracted from the figure (R = 1.96 [Ω]), however is slightly higher than the values found in table 4.1. This could be due to the current sensors having finite resistance that adds to the total resistance, or due to human error during read-out. For significantly higher inductance values, phase lag is present, and the linear model becomes invalid. In that case current control is required for Field Oriented Control.

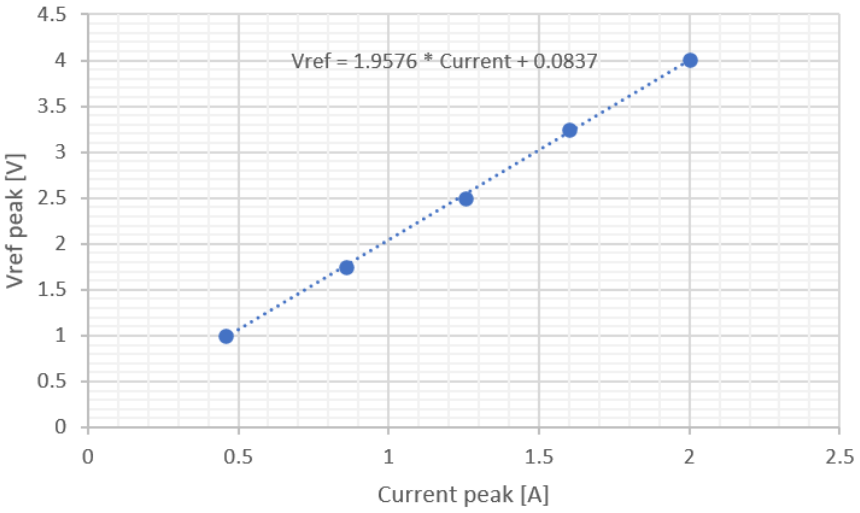

Figure 4.3: The relation between the current and the potential of a single phase.

4.3 Measuring Motor Constant

Using the above linear relation between the current and the potential, a three phase signal of constant 1 [A] DC equivalence using SVPWM is fed to the motor, such that the carriage constantly accelerates. This allows for measuring the motor constant by using an analog force gauge shown in figure 4.4. The carriage is held, such that the carriage does not accelerate. The motor force gauge is positioned next to the carriage, as close to the stator as possible. The carriage is then let go, and the peak force is measured. This is repeated for four random positions along the stator (table 4.2.

Figure 4.4: An analog force gauge is used to measure the motor constant.

In order to calculate the motor constant, the friction force is required. The motor is turned off and the demonstrator is put under angle until the carriage starts sliding down. This happened at an angle of 12 degrees, which corresponds to a friction constant of 0.21 ($\mu_s = tan^{-1}\alpha$). Since the carriage in its entirety weighs 0.37 [kg], the static friction force is thus 0.75 [N]. The motor constant can then be calculated by adding the static friction to the average measured force. The motor constant is found to be about 4.05 [$\frac{N}{A}$], which is 8 % higher than the value found in the COMSOL model (3.75 [N]). However, this could be explained since the motor is currently using SVPWM, whereas the COMSOL model uses SPWM. As explained in section 2.5.3, SVPWM can output up to 15 % more power compared to SPWM.

Equivalent DC current per phase	1 [A]

Random position	1	2	3	4
Measured force	3.5 [N]	3 [N]	3.3 [N]	3.5 [N]
Average measured fore	3.3 [N]			

Friction force	0.75 [N]

Motor constant (Friction + Measured force)	4.05 [N]

Table 4.2: Using an analog force gauge, the output force has been measured. Friction is added to determine the motor constant.

4.4 Black Box Identification

The plant used in the SIMULINK Control model in section 3.6 first represented a mass system that is in the form 'X/F' (position/peak actuator force). The force is then converted to a current, which is then converted to a voltage that is used for SVPWM commutation.

Since the relation between the current and the potential is found to be linear in the previous section, this relation and the motor constant are no longer required in the control loop that was presented in section 3.6. The plant is now in the form 'X/V' (position/peak voltage), which reduces the errors within the control loop, since the previous found current/potential relation and motor constant were determined separately and experimentally.

A three phase chirp signal (10 to 100 [Hz]) with a peak voltage of 3 [V] is fed to the motor (input) and the new position is saved right after (output). The program samples at 800 [Hz]. These arrays are saved and imported in Matlab. Using the following code a bode plot of 'X/V' can be found:

```
clear;
clc;
Fs = 1000;
csv = table2array(readtable('inputoutput.csv', 'Delimiter', ';'));
ip = csv(:, 2);
op = csv(:, 3);
[T, f] = tfestimate(ip, op, [], [], [], Fs);
[C, f] = mscohere(ip, op, [], [], [], Fs);
[funcmag, funcphase, funcwout] = bode(tf([1], [0.068 0 0]), 'w', [2 * pi 150 * 2 * pi]);
figure(1);
subplot(3, 1, 1);semilogx(f, 20*log10(abs(T)));
xlabel('Frequency [Hz]');
ylabel('Magnitude [X/V]');
hold on;
subplot(3, 1, 1);semilogx(funcwout/(2 * pi), 20*log10(abs(squeeze(funcmag))));
xlim([1 200]);
subplot(3, 1, 2);semilogx(f, radtodeg(angle(T)));
xlabel('Frequency [Hz]');
ylabel('Phase [deg]');
subplot(3, 1, 3);semilogx(f, C);
xlabel('Frequency [Hz]');
ylabel('Consistency');
```

Figure 4.5: Black box identification code.

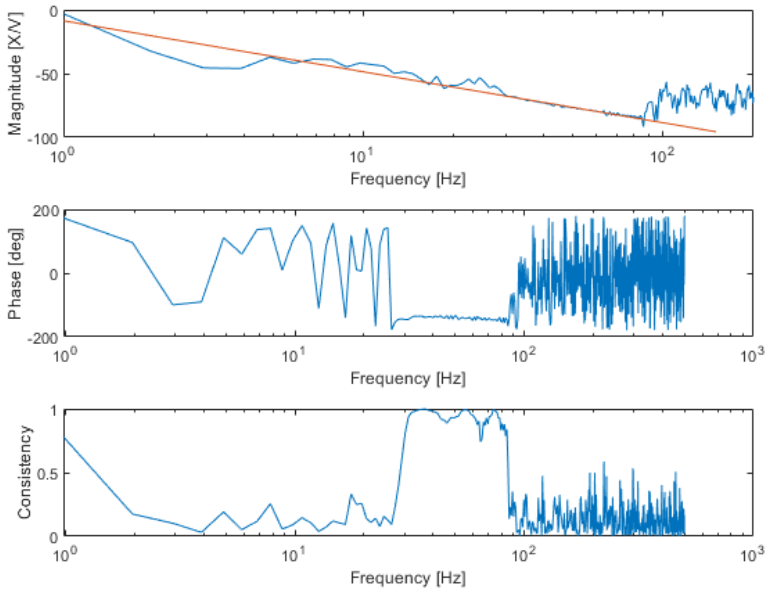

Figure 4.6: Black box identification [X/F]. The red line in the magnitude plot shows a 'mass' system that is $X/V = \frac{1}{0.068s^2}$.

It can be seen that the signal is not a clean mass system that is of the form $X/V = \frac{1}{ms^2}$, where 'm' is the mass; 'X' the position and 'V' the peak voltage of the three phase signal. This could be due to SVPWM, since the inductance is not large enough to smoothed'out the waveform to

a sine wave (as explained in section 2.5.3), resulting in a non-clean sinusoidal input. This effect is more present at lower frequencies. Furthermore, at low frequencies, the mass line could also have jitter due to influence of wire that introduces stiffness.

The magnitude mass line is however rather constant starting from 30 [Hz] and has good consistency over a range of 30 to 80 [Hz]. This line is extrapolated to the other frequencies and corresponds to a mass system with 'm' = 0.068. The following PD rule-of-thumb is applied for this mass system:

$K_t = \frac{1}{|plant|_w}$
$K_p = K_t/3$
$D = \frac{\frac{1}{w}}{3}$

Here 'w' is the bandwidth frequency the controller is designed for and $|plant|_w$ the magnitude at bandwidth. In the SIMULINK model in Appendix C6, 'Kdx' = 'K_p' and 'Dx' = 'D'. Since a mass system is considered, a PD controller introduces enough phase margin and suffices for feed-back position control, i.e. 'Ix' in the SIMULINK control model is zero. The controller is designed for 130 [Hz] bandwidth and tested for different trapezoidal motion profiles in the next section. The control loop operates at 500 [Hz] and the PWM signals operate at 20 [kHz] (inaudible).

4.5 Positioning Results & PD Damper

The motor is programmed such that the Arduino accepts step and direction signals. These are then converted by the motor's Arduino to a position that is to be tracked. This makes the motor plug-and-play to any low-duty CNC machine. The motor's Arduino is hooked up to another Arduino that is programmed to output trapezoidal motion profiles at 30 steps/mm.

The trapezoidal motion profiles have an acceleration of 10 $[\frac{m}{s^2}]$ and a maximum speed of 1 $[\frac{m}{s}]$. Three different 'step' sizes are studied, namely 10 [mm]; 50 [mm] and 200 [mm]. The overshoot and the settled off-set are of interest and provide accuracy information (see figure 4.7. These errors are calculated as Error = Set position - position.

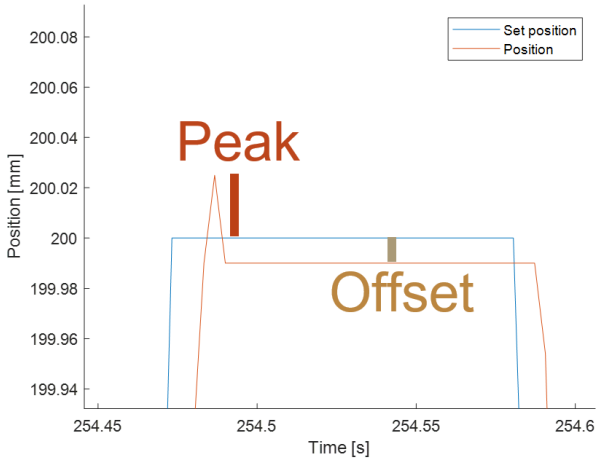

Figure 4.7: The peak and settled off-set values are of interest, the error is defined as Error = Set position - position.

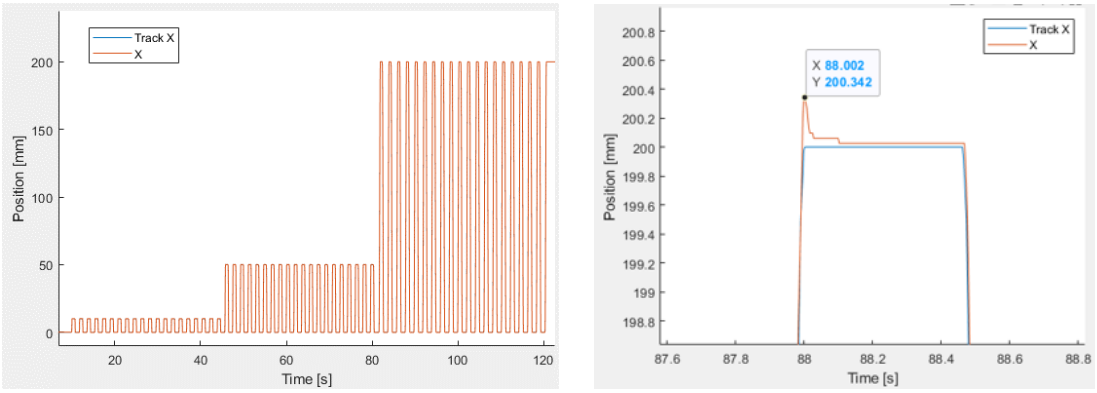

(a) **(b)**

Figure 4.8:
(a) The motor is moved back and forth 20 times for each step size (b) A high peak is found with the standard PD controller.

Initially, for each step size the motor moves forth and back 20 times to study the motion (see figure 4.8a). Zooming in on one of the motion trapezoidal motion profiles, we find a peak error of 0.34 [mm].

Multiple methods were tried to reduce this error:

1. Increase Damper of the PD controller.
2. Lower Proportional considerably, due to possible first mode.
3. Gain scheduling, a method where the input error (of the PD controller) is modified close to the final position, such that the output force is modified accordingly.

However, none of these methods seem to do the trick. After an in-depth analysis and some troubleshooting, the issue was found to be 'Derivative kick' [4]. The derivative takes the derivative on the error as:

$$\frac{dError}{dt} = \frac{dSetposition}{dt} - \frac{dPosition}{dt} \tag{4.1}$$

However, in the case of a step signal (which is similar in this case), the first term ($\frac{dSetposition}{dt}$) becomes very large. This increases the D-action considerably and outputs a force that causes the spike seen in figure 4.8b. By removing this first term, and just taking the error on the current position as input for the D-action, solves the issue and removes the spike (see figure 4.9). Whenever the set position is constant, this winds up to a perfect solution, however during motion the D-action does not output the correct damping. This is found to be acceptable since the transition time from one position to the other is a merely 0.15 [s] (see figure 4.10b). This method is called taking 'the derivative on measurement' and is often used in high-speed industrial applications [4].

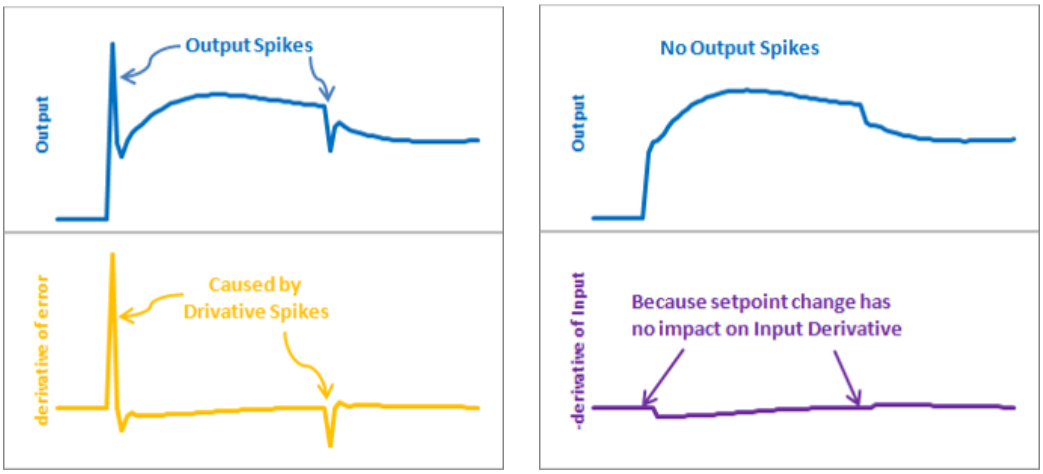

(a) **(b)**

Figure 4.9:
(a) By taking the derivative on error, the derive on the input may cause a derivative spike. By only taking the derivative on the measurement as in (b), the derivative spike is removed [4].

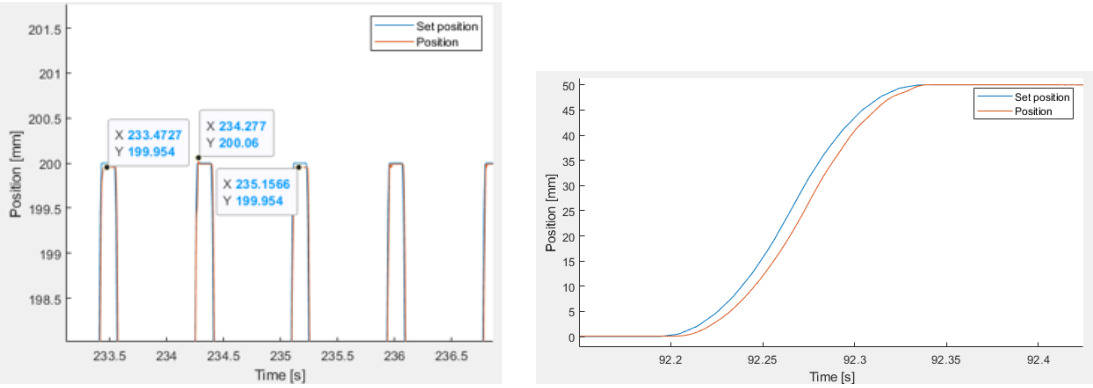

(a) **(b)**

Figure 4.10:
(a) The derivative spike has disappeared after taking the derivative on the measurement only. However as can be seen in (b), this results in reduced tracking performance during motion.

Finally, the motor moves back and forth a 100 times for each step size and the peak and settled offset values are processed in Matlab (see script appendix C8: Positioning results post-processing). The averages and standard deviations of each step size are shown in figure 4.11:

```
10 mm steps, 1m/s, 10m/s^2, 1 to 3 sigma

mu_error_10mm_peak =

  -1.9000e-04


sigma_10mm_peak =

    0.0019
    0.0038 95%
    0.0057 99%


mu_error_10mm_offset =

    0.0502


sigma_10mm_offset =

    0.0523
    0.1045 95%
    0.1568 99%
```

```
50 mm steps, 1m/s, 10m/s^2, 1 to 3 sigma

mu_error_50mm_peak =

   -0.0375


sigma_50mm_peak =

    0.0561
    0.1122 95%
    0.1683 99%


mu_error_50mm_offset =

   -0.0093


sigma_50mm_offset =

    0.0197
    0.0394 95%
    0.0592 99%
```

```
200 mm, 1m/s, 10m/s^2, 1 to 3 sigma

mu_error_200mm_peak =

   -0.0143


sigma_200mm_peak =

    0.0352
    0.0704 95%
    0.1055 99%


mu_error_200mm_offset =

    0.0443


sigma_200mm_offset =

    0.0540
    0.1080 95%
    0.1620 99%
```

Figure 4.11: The averages and standard deviations of each step size.

It can be seen that the final accuracy has increased significantly. The motor may be classified as industrial, since the final motor accuracy is in the range of 0.2 [mm] [50].

4.6 Conclusion: Validation & Experiments

In this chapter the demonstrator was presented, that consists of low-cost components. The coils were validated and the linear relationship between peak current and peak potential was determined, which is used in the MATLAB SIMULINK control model. This linear implementation is allowed, since the inductance is insignificant, causing essentially no phase lag. Furthermore, the PWM frequency used is constant. The experimentally found values differed slightly from the simulated coil parameters, however this could be explained due to a different (unknown) fill factor of the 0.5 [mm] wire.

The motor constant was determined and validated. The motor constant was found to be 4.05 $[\frac{N}{A}]$, which is 8% higher than what was simulated in the COMSOL Motor model. This may be explained due to the use of SVPWM over SPWM. SVPWM increases the performance of the motor up to 15 %, as explained in section 2.5.3.

A black box identification had been performed using a chirp signal (10 to 100 [Hz]), which simplified and improved the control scheme, since the experimentally found motor constant and the linear relation between the current and the potential were no longer used. This allows for a tighter control loop with improved performance, which simplified the plant from 'X/Fpeak' to 'X/Vpeak'. PD values for 130 [Hz] bandwidth using the rule of thumb (paragraph 4.3) were tuned for closed-loop position control. The control loop operates at 500 [Hz] and the PWM signals operate at 20 [kHz] in order to be inaudible.

Three different trapezoidal motion profiles were discussed: 10 [mm], 50 [mm] and 200 [mm] at an acceleration of 10 $[\frac{m}{s^2}]$ and a maximum speed of 1000 $[\frac{m}{s}]$. After taking the derivative on the measurement for the Damper of the PD controller, the final position accuracy was found to be close to 0.2 [mm] 3 σ, which is of industrial grade positioning.

Chapter 5

Conclusion & Discussion

5.1 General Conclusion

In this Thesis report, 'the design and manufacturing of a low-cost direct-drive motor' was discussed. The main conclusion is that the project had been a success. An iron-less tubular is developed that is able to achieve industrial positioning (0.2 [mm] accuracy) at an acceleration of 10 $[\frac{m}{s^2}]$ with a maximum speed of 1000 $[\frac{mm}{s}]$. The model had been optimized given the constraints shown in section 3.2.

5.1.1 Problem Definition

In the General Introduction of this report, the issues that come with belt-driven systems were discussed. Due to the elasticity of the belt, vibrations and belt-stretch are introduced, which limits the maximum acceleration of the drive system. Furthermore, since the drive system utilizes multiple pulleys and transmissions, these introduce mechanical issues such as backlash and creep, and complicate the assembly process. From the existing solutions it was found that direct-drive motors, and in particular linear motors would be a prosperous replacement.

5.1.2 Theory

An in-depth introduction regarding linear motors was provided. The physical principle had been explained based on the Lorentz actuator and information regarding cogging is given. Furthermore, commutation, the switching of the coil currents and Field Oriented Control had been explained in-depth.

Different linear motor types were discussed regarding their working and State-of-the-Art. A morphological overview helped to find the the most prosperous motor type for this application. It was found that the iron-less tubular linear motor is the most prosperous candidate, because of its high efficiency; high actuator stiffness; no cogging; great heat dissipation; non-critical air gap; ease of manufacturing and a very wide speed range. Furthermore, the rotor can easily be incorporated in a carriage with sliding bearings, where the stator also acts as the guiding rod that is part of the gantry. This reduced the complexity and assembly cost of the gantry significantly.

5.1.3 Design & Optimization

The iron-less tubular linear motor was optimized given the constraints and objectives in section 3.2.

A time-dependent COMSOL generator provided information regarding motor behavior and phase wiring. The motor constant could be extracted from the results, and was used for validation. A stationary COMSOL motor model was then used to reduce on computation time to extract the motor constant and was extended to a parametric sweep study intended for the brute force optimization. The motor constant and coil resistance of 1536 different motor models were used in MATLAB for post-processing.

The optimization yielded a list of optimized motor models that fit the constraints, and the choice fell on an actuator that has a motor constant of approximately 3.75 $[\frac{N}{A}]$; a phase resistance of 2.2 $[\Omega]$; a power usage of approximately 20 $[W]$ and requires an equivalent DC current of approximately 1.7 $[A]$.

The carriage was designed such that assembly is made easy. The carriage was 3D printed from 1 part that is of heat-resistant material of up to 165 degrees Celcius. A 30 $[mm]$ cooling fan was included to cool the motor and slide bearings were used that can easily be glued in. The rotor was also 3D printed from a single part, around which the coils were wound using a coil winding machine with 0.5 $[mm]$ wire. The stator uses the 1.4 [T] NdFeB permanent magnets with 3D printed spacers and are held in place using two 3D printed caps. The stator's tube is made of brass, which has compared to aluminium or copper reduced eddy current damping.

The total material cost that includes material; encoder and PCB for 0.5 $[m]$ stroke is approximately 60 euros, which is a huge improvement over outsourcing these motors elsewhere (700 euros at Tecnotion).

5.1.4 Validation

Using a force gauge and by measuring the friction force, the motor constant was determined to be 4.05 $[\frac{N}{A}]$, which was an 8% increase on the simulated force. This may be due to SVPWM, which outputs up to 15% more peak current compared to SPWM used in the COMSOL simulation model.

The experimentally found resistance of a single coil was found to be slightly smaller, however may be explained due to a different (unknown) fill factor of the wire. The insulation layer was taken as 25 $[\mu m]$.

A black box identification had been performed using a chirp signal of 10 to 100 [Hz] to find the plant 'X/Vpeak'. Vpeak is the peak voltage of the 3 phase signal. PD values for 130 [Hz] bandwidth using the rule of thumb (paragraph 4.3) were tuned for closed-loop position control. The control loop operates at 500 [Hz] and the PWM signals operate at 20 [kHz] in order to be inaudible.

Using an external Arduino, three different trapezoidal motion profiles were performed: 10 [mm], 50 [mm] and 200 [mm]. The acceleration was set to 10 $[\frac{m}{s^2}]$ and the maximum speed was set to 1000 $[\frac{mm}{s}]$. The external Arduino output step and direction signals at 30 steps/mm that are converted to position information. After taking the derivative on the measurement for the

Damper of the PD controller, the final position accuracy was found to be close to 0.2 [mm] 3 σ, which is of industrial grade positioning.

5.2 Discussion

5.2.1 Field Oriented Control

In this report, Field Oriented Control was discussed in detail. However, no current control is implemented to achieve Field Oriented Control in the current design. Since the inductance of the electromagnetic coils were found to be very small, virtually no phase lag was present and the current appeared to follow ohm's law. Furthermore, since the PWM frequency is constant, this resulted in a linear relation between the current and the potential.

The code however does include angle (of the electrical cycle) data that is used in the SVPWM algorithm to properly commutate the motor. The question may then arise whether this may also be considered Field Oriented Control, since no current control is implemented. However, since no current control was found to be required, yet proper alignment with the magnetic field was achieved, it was assumed Field Oriented Control was implemented.

5.2.2 Analytical Model

In this report the analytical model is provided, however is not used for further development. There were some issues in evaluating the triple integral numerically, which could have been resolved, however a better approach was to use finite-elements. This allowed for a detailed study on the motor's behavior. Nonetheless, the analytical model provides detailed information on the physics used in the COMSOL motor model and is in that sense very useful.

5.2.3 Influence Of Wiring

As can be seen in the demonstrator model, bundles of cables are present. These theoretically introduce a stiffness to the plant, which may worsen control performance that uses a controller based on a mass system. The effect of these cables were not taken into account, since it was assumed the required force to move the cables is insignificant compared to the required force for accelerating the carriage. For larger machines, this effect may be more significant, due to the increase in cable mass and a more present first mode.

5.2.4 Measurement Set-up

The black box identification uses the design's own measurement system. In the case the motor is implemented in a gantry, that uses two y-axes and one x-axis, the gantry requires to be sufficiently stiff in order to still be able to achieve industrial positioning (0.2 $[mm]$) on the x-axis. Otherwise a different measurement set-up is required, where the encoder strip is figuratively speaking attached to the static world, such that a controller could be designed that incorporates the transverse stiffness of the y-axis.

Furthermore, the demonstrator uses 3D printed components that are made of PLA and similar. These are materials of low elastic modulus. In order to counter significant deflection, these components are designed thick, such that the area moment of inertia is sufficiently large. However, the significance of this effect was not studied.

Chapter 6

Appendices

6.1 Appendix A: SVPWM Sector Calculations

Sectors (n)	Upper switching (S_1, S_3, S_5)	Lower switching (S_4, S_6, S_2)
1	$S_1 = T_1 + T_2 + \frac{T_0}{2}$ $S_3 = T_2 + \frac{T_0}{2}$ $S_5 = \frac{T_0}{2}$	$S_4 = \frac{T_0}{2}$ $S_6 = T_1 + \frac{T_0}{2}$ $S_2 = T_1 + T_2 + \frac{T_0}{2}$
2	$S_1 = T_1 + \frac{T_0}{2}$ $S_3 = T_1 + T_2 + \frac{T_0}{2}$ $S_5 = \frac{T_0}{2}$	$S_4 = T_2 + \frac{T_0}{2}$ $S_6 = \frac{T_0}{2}$ $S_2 = T_1 + T_2 + \frac{T_0}{2}$
3	$S_1 = \frac{T_0}{2}$ $S_3 = T_1 + T_2 + \frac{T_0}{2}$ $S_5 = T_2 + \frac{T_0}{2}$	$S_4 = T_1 + T_2 + \frac{T_0}{2}$ $S_6 = \frac{T_0}{2}$ $S_2 = T_1 + \frac{T_0}{2}$
4	$S_1 = \frac{T_0}{2}$ $S_3 = T_1 + \frac{T_0}{2}$ $S_5 = T_1 + T_2 + \frac{T_0}{2}$	$S_4 = T_1 + T_2 + \frac{T_0}{2}$ $S_6 = T_2 + \frac{T_0}{2}$ $S_2 = \frac{T_0}{2}$
5	$S_1 = T_2 + \frac{T_0}{2}$ $S_3 = \frac{T_0}{2}$ $S_5 = T_1 + T_2 + \frac{T_0}{2}$	$S_4 = T_1 + \frac{T_0}{2}$ $S_6 = T_1 + T_2 + \frac{T_0}{2}$ $S_2 = \frac{T_0}{2}$

Figure 6.1: Source: [1]

6.2 Appendix B: SVPWM Algorithm

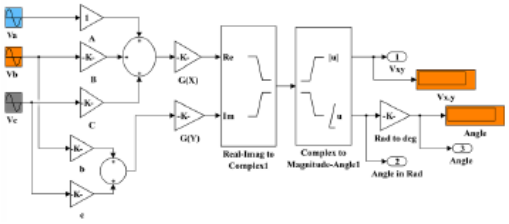

Illustrates of implementation of (V_{xy}) and angle (θ).

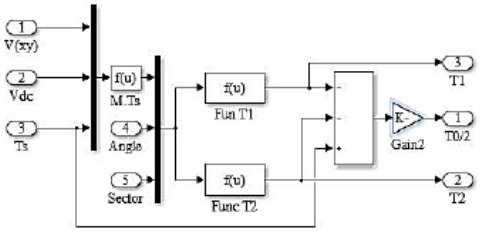

Implementation the (T_1, T_2 & $T_0/2$)

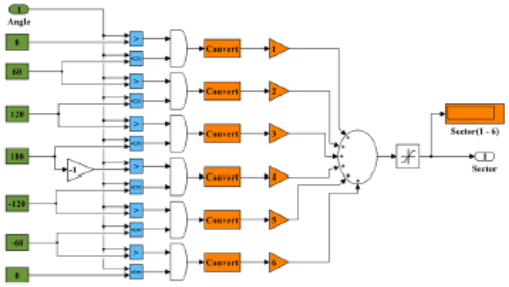

Blocks to generate six sectors (1 to 6).

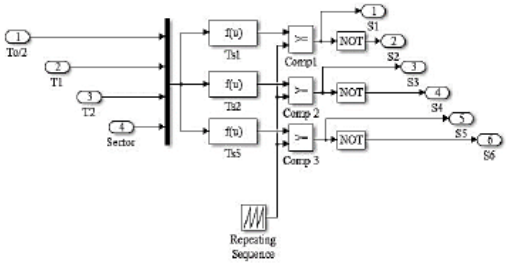

Implementation the transistor switching signal (S_1 to S_6).

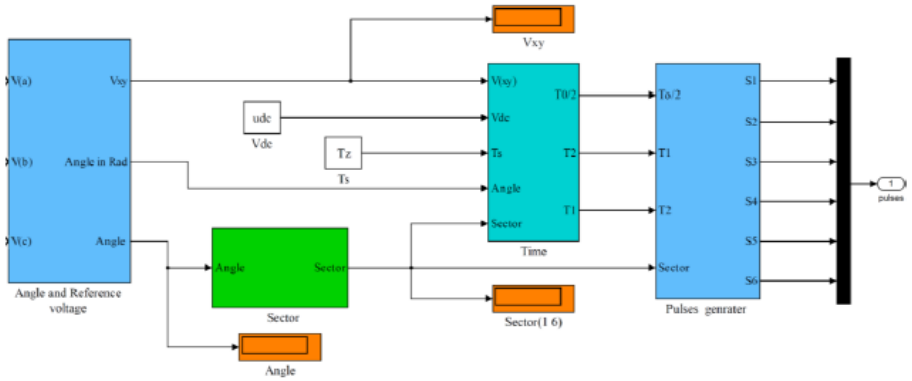

Blocks model to the SVPWM based on the sector selection technique.

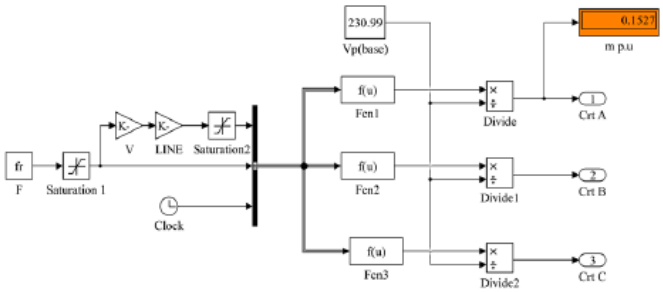

MATLAB/ SIMULINK blocks shown, how can calculate (V/f) ratio.

Figure 6.2: Source: [1]

6.3 Appendix C: Field Oriented Control PI Control

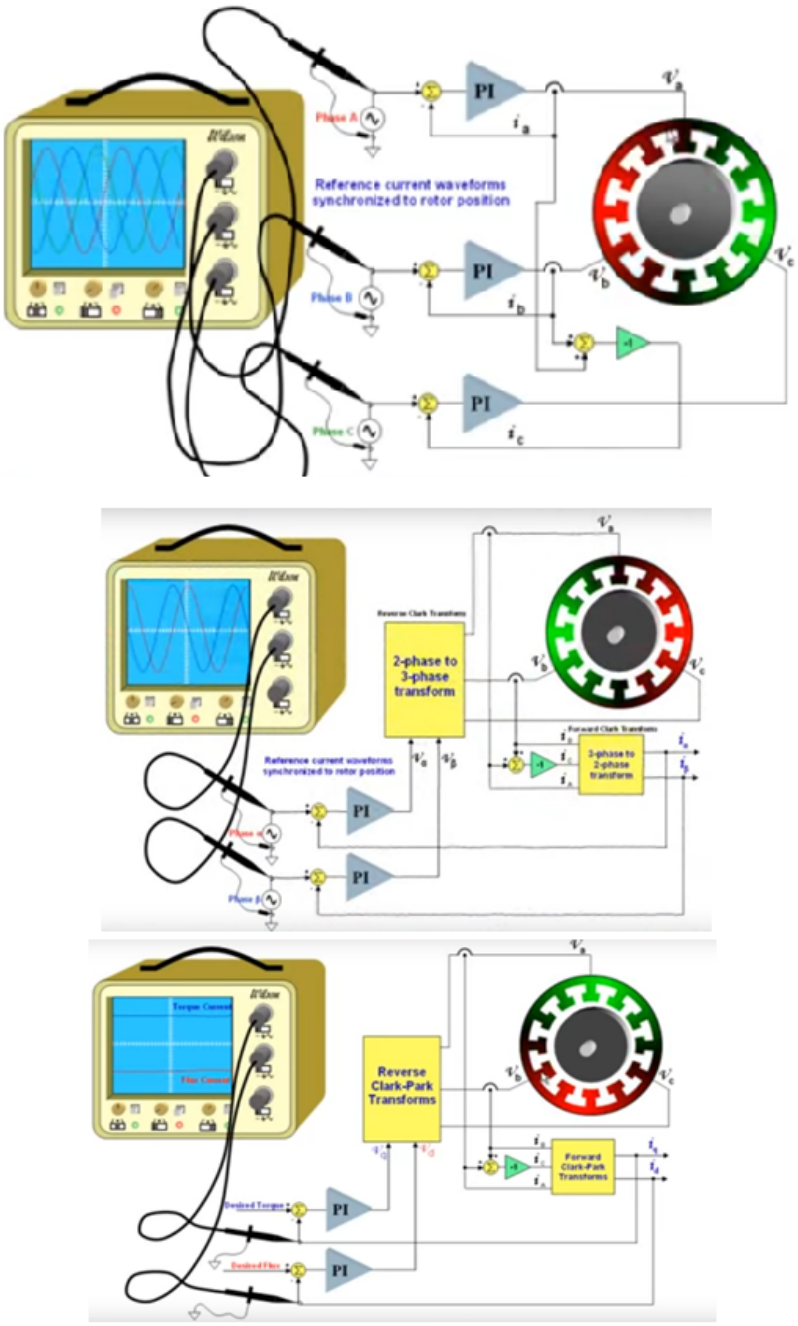

Figure 6.3: Source: [32]

6.4 Appendix D: Morphological Overview

	Thrust	Cogging	Weight	Production cost (w. assembly)	Efficiency	Total
Iron-core slotted flat	5	2 (reducable)	2	3	5	17
Iron slotless flat	4	2 (reducable)	3	3	4	16
Ironless slotless flat	2	5	4	3	3	17
SLIM/DLIM	1	5	1	1	1	9
U-Channel	3	5	5	2	2	17
Tubular	4	5	5	4	4	22

Bibliography

[1] A. K. Ali. "Simulation and Study of SVPWM Inverter for (VFD) Applications". In: (2017).

[2] Aventics. *Stangloze cilinders, RTC-serie*. URL: https://www.aventics.com/en/products/pneumatic-products/pneumatic-cylinders-drives-and-grippers/stangloze-cilinders/stangloze-cilinders-rtc-serie/?no_cache=1. (accessed: january 2020).

[3] Bangood. *400 mm CNC stroke*. URL: https://de.banggood.com/400mm-Stroke-Actuator-CNC-Linear-Motion-Lead-Screw-Slide-Stage-with-42-Stepper-Motor-p-1162135.html?cur_warehouse=CN. (accessed: january 2020).

[4] B. Beauregard. *Improving the Beginner's PID – Derivative Kick*. URL: https://brettbeauregard.com/blog/2011/04/improving-the-beginner%E2%80%99s-pid-derivative-kick/. (accessed: january 2020).

[5] M. Binnard. *Planar motor with linear coil arrays*. URL: https://patents.google.com/patent/US6452292B1/en?oq=US6452292B1. (accessed: january 2020).

[6] M. Binnard. *Planar motor with linear coil arrays*. URL: https://patents.google.com/patent/US6445093B1/en?oq=US6445093B1. (accessed: january 2020).

[7] Aerotech blog. *What is commutation and how does it affect linear motor performance?* URL: http://blog.aerotechmotioncontrol.com/2012/08/08/commutation-and-linear-motors/. (accessed: january 2020).

[8] G. S. Boast. *Coaxial linear motor for extended travel*. URL: https://patents.google.com/patent/US6313552B1/en?oq=US6313552B1+. (accessed: january 2020).

[9] M. Budimir. *Micro-stepping Myths*. URL: https://www.machinedesign.com/archive/article/21812154/microstepping-myths. (accessed: january 2020).

[10] D. Collins. *How are servo motors physically different from motors that run open loop?* URL: https://www.motioncontroltips.com/faq-how-are-servo-motors-physically-different-from-motors-that-run-open-loop/. (accessed: january 2020).

[11] D. Collins. *How do magnetic linear encoders differ from optical versions?* URL: https://www.linearmotiontips.com/how-do-magnetic-linear-encoders-differ-from-optical-versions/. (accessed: january 2020).

[12] D. Collins. *Low-profile linear stepper motor stage from H2W Technologies*. URL: https://www.linearmotiontips.com/low-profile-linear-stepper-motor-stage-from-h2w-technologies/. (accessed: january 2020).

[13] D. Collins. *What are capacitive encoders and where are they suitable?* URL: https://www.motioncontroltips.com/faq-what-are-capacitive-encoders-and-where-are-they-suitable/. (accessed: january 2020).

[14] D. Collins. *What are linear stepper motors?* URL: https://www.linearmotiontips.com/faq-what-are-linear-stepper-motors/. (accessed: january 2020).

[15] D. Collins. *What do Lissajous figures tell us about encoder output?* URL: https://www.motioncontroltips.com/what-do-lissajous-figures-tell-us-about-encoder-output/. (accessed: january 2020).
[16] D. Collins. *What is cogging in linear motors?* URL: https://www.linearmotiontips.com/what-is-cogging-in-linear-motors/. (accessed: january 2020).
[17] D. Collins. *What is linear motor commutation?* URL: https://www.linearmotiontips.com/what-is-linear-motor-commutation/. (accessed: january 2020).
[18] Machine Design. *Linear AC Motors.* URL: https://www.machinedesign.com/motors-drives/article/21812653/linear-ac-motors. (accessed: january 2020).
[19] Etel. *Linear motors overview.* URL: https://www.etel.ch/linear-motors/overview/. (accessed: january 2020).
[20] First4magnets. *Neodymium magnet grades.* URL: https://www.first4magnets.com/tech-centre-i61/information-and-articles-i70/neodymium-magnet-information-i82/grades-of-neodymium-magnets-i92. (accessed: january 2020).
[21] J. G. Floresta. *High performance ironless linear motor with supported windings.* URL: https://patents.google.com/patent/US6239516B1/en?oq=US6239516B1+. (accessed: january 2020).
[22] L. Grant. *Precision DIY Calipers? That's A Moire!* URL: https://hackaday.com/2018/03/07/0-05-mm-precision-thats-a-moire/. (accessed: january 2020).
[23] T. J. Harned. *Linear motor with magnet rail support, end effect cogging reduction, and segmented armature.* URL: https://patents.google.com/patent/US6919654B2/en?oq=US6919654B2. (accessed: january 2020).
[24] A. J. Hazelton. *Magnet array for a shaft-type linear motor.* URL: https://patents.google.com/patent/US6313551B1/en?oq=US6313551B1+. (accessed: january 2020).
[25] A. J. Hazelton. *Planar electric motor and positioning device having transverse magnets.* URL: https://patents.google.com/patent/US6285097B1/en?oq=US6285097B1. (accessed: january 2020).
[26] A. J. Hazelton. *Wafer positioner with planar motor and mag-lev fine stage.* URL: https://patents.google.com/patent/USRE41232E1/en?oq=USRE41232E1. (accessed: january 2020).
[27] A. J. Hazelton. *Wedge and transverse magnet arrays.* URL: https://patents.google.com/patent/US6188147B1/en?oq=US6188147B1+. (accessed: january 2020).
[28] K. Horiike. *Linear motor and manufacturing method thereof.* URL: https://patents.google.com/patent/JP4860222B2/en?oq=JP4860222B2. (accessed: january 2020).
[29] B. Horwitz. *Diffractive techniques improve encoder performance.* URL: https://www.laserfocusworld.com/detectors-imaging/article/16549031/diffractive-techniques-improve-encoder-performance. (accessed: january 2020).
[30] Prototype Hubs. *CNC Router.* URL: https://prototypehubs.com/cnc-machining/. (accessed: january 2020).
[31] Rigid Ink. *The Ultimate 3D Print Quality Troubleshooting Guide 2019.* URL: https://rigid.ink/pages/ultimate-troubleshooting-guide#issue-vibrations-and-3d-printing-ringing-31. (accessed: january 2020).
[32] Texas Instruments. *Field Oriented Control of Permanent Magnet Motors.* URL: https://www.youtube.com/watch?v=cdiZUszYLiA. (accessed: january 2020).
[33] N. Ishiyama. *Linear motor equipped with a stator which is easily assembled.* URL: https://patents.google.com/patent/EP0878899A1/en?oq=EP0878899A1+. (accessed: january 2020).
[34] Inc. K&J Magnetics. *Halbach Arrays.* URL: https://www.kjmagnetics.com/blog.asp?p=halbach-arrays. (accessed: january 2020).

[35] J. Kelly. *What is the Most Effective Way to Commutate a BLDC Motor?* URL: https://www.digikey.nl/en/articles/what-is-the-most-effective-way-to-commutate-a-bldc-motor. (accessed: january 2020).
[36] Z. Khan. *What is the difference between absolute and incremental encoders?* URL: https://www.motioncontroltips.com/faq-what-is-the-difference-between-absolute-and-incremental-encoders/. (accessed: january 2020).
[37] H. J. Kim. *Xyz-axes table.* URL: https://patents.google.com/patent/EP1330864B1/en?oq=EP1330864B1. (accessed: january 2020).
[38] D. Kirsh. *Types of linear motors.* URL: https://www.medicaldesignandoutsourcing.com/types-linear-motors/. (accessed: january 2020).
[39] R. Leach. *Optical encoders.* URL: https://www.sciencedirect.com/topics/engineering/optical-encoders. (accessed: january 2020).
[40] J. van der Linde. "Classical Electromagnetic Theory". In: (2nd edition).
[41] How to Mechatronics. *How Rotary Encoder Works and How To Use It with Arduino.* URL: https://www.youtube.com/watch?v=v4BbSzJ-hz4. (accessed: january 2020).
[42] Precision Microdrives. *Cogging torque in permanent magnet motors.* URL: https://www.precisionmicrodrives.com/content/cogging-torque-in-permanent-magnet-motors/. (accessed: january 2020).
[43] B. C. Murphy. "DESIGN AND CONSTRUCTION OF A PRECISION TUBULAR LINEAR MOTOR AND CONTROLLER". In: (2003).
[44] E. Nolle. *Multi-phase transverse magnetic flux machine.* URL: https://patents.google.com/patent/US5854521A/en?oq=US5854521A. (accessed: january 2020).
[45] Prof. S. K. Patil. "Implementation of SVPWM Based Three Phase Inverter Using 8 Bit Microcontroller". In: (2015).
[46] Prusa. *Prusa MK3.* URL: https//prusa3d.com/. (accessed: january 2020).
[47] Nippon Pulse. *Linear Motor Systems: Iron Core, U-Channel, and Tubular Linear Motors.* URL: https://www.nipponpulse.com/learning/white-papers/linear-motor-systems-iron-core-u-channel-and-. (accessed: january 2020).
[48] Jr R. Pulford. *Method of magnetizing the shaft of a linear stepper motor.* URL: https://patents.google.com/patent/US7752736B2/en?oq=US7752736B2. (accessed: january 2020).
[49] Rep Rap. *CoreXY.* URL: https://reprap.org/wiki/CoreXY. (accessed: january 2020).
[50] B. Redwood. *Dimensional accuracy of 3D printed parts.* URL: https://www.3dhubs.com/knowledge-base/dimensional-accuracy-3d-printed-parts/. (accessed: january 2020).
[51] Roboteq. *Field Oriented Control.* URL: https://www.roboteq.com/technology/field-oriented-control. (accessed: january 2020).
[52] H. Daepp S. DeHart S. Chopra. *Motors.* URL: https://www.slideserve.com/Audrey/main-features. (accessed: january 2020).
[53] T. H. E. Scheepers. *Linear induction machines for planar positioning.* TU Delft, 2017.
[54] R. M. Schmidt. "The Design of High Performance Mechatronics". In: (2nd revised edition).
[55] Sentech. *Inductive encoder: accurately measure displacement in harsh conditions.* URL: https://www.sentech.nl/en/sensor-technology/inductive-encoder-accurately-measure-displacement-in-harsh-conditions. (accessed: january 2020).
[56] Innovation services. *Comparative evaluation of Lorentz and reluctance actuators.* URL: https://www.innovationservices.philips.com/looking-expertise/high-precision-engineering/comparative-evaluation-of-lorentz-and-reluctance-actuators/. (accessed: january 2020).

[57] P. Smit. *Forcer and associated three phase linear motor system.* URL: https://patents.google.com/patent/US6522035B1/en?oq=US6522035B1+. (accessed: january 2020).
[58] Blue sea systems. *Electrical Conductivity of Materials.* URL: https://www.bluesea.com/resources/108/Electrical_Conductivity_of_Materials. (accessed: january 2020).
[59] Y. Tang. *Tubular linear motor.* URL: https://patents.google.com/patent/US9379599B2/en?oq=US9379599B2+. (accessed: january 2020).
[60] A. Toushioki. *Linear motor and linear guide apparatus.* URL: https://patents.google.com/patent/KR101018521B1/en?oq=KR101018521B1+. (accessed: january 2020).
[61] Techno Trip. *Sine PWM inverter Simulink model, SPWM in Simulink.* URL: https://www.youtube.com/watch?v=mSbJj_TBGd8&app=desktop. (accessed: january 2020).
[62] Ultimaker. *Ultimaker's drive system.* URL: https://www.ultimaker.com. (accessed: january 2020).
[63] Vulcaman. *DIY Ironless Linear Servo-motor.* URL: https://www.instructables.com/DIY-IRONLESS-LINEAR-SERVO-MOTOR/. (accessed: january 2020).
[64] B. C. Murphy W. J. Kim. "Development of a Novel Direct Drive Tubular Linear Brushless Permanent-Magnet Motor". In: (2004). URL: https://ieeexplore.ieee.org/document/1257779.
[65] Wikiwand. *Linear motor.* URL: https://www.wikiwand.com/en/Linear_motor. (accessed: january 2020).
[66] K. Yanagi. *Coreless linear motor of two-degrees-of-freedom.* URL: https://patents.google.com/patent/JP2011193553A/en?oq=JP2011193553A+. (accessed: january 2020).
[67] K. Yoshiaki. *Linear motor.* URL: https://patents.google.com/patent/KR100726533B1/ko?oq=KR100726533B1+. (accessed: january 2020).